ELSEVIER

Coordination Chemistry Reviews
219–221 (2001) 993–1032

COORDINATION CHEMISTRY REVIEWS

www.elsevier.com/locate/ccr

Assignment of the optical spectra of metal phthalocyanines through spectral band deconvolution analysis and ZINDO calculations

John Mack, Martin J. Stillman *

Department of Chemistry, University of Western Ontario, London, Ontario, Canada, N6A 5B7

Received 18 December 2000; accepted 25 May 2001

Contents

Abstract

The optical spectra of the porphyrins and phthalocyanines are dominated by the $\pi\rightarrow\pi^{*}$ bands associated with the heteroaromatic, 16 atom, 18 π-electron inner perimeter cyclic

* Corresponding author. Tel.: +1-519-6613821; fax: +1-519-6613022.
E-mail address: martin.stillman@uwo.ca (M.J. Stillman).

PII: S0010-8545(01)00394-0

polyene. Despite experimental measurements spanning over 60 years, no model exists that completely accounts for all bands in the UV–vis–near IR regions in each of the accessible redox states of many of these ring compounds. Spectral data for many neutral porphyrin and phthalocyanine compounds with a range of metals, axial and peripheral substituents have been reported from absorption and magnetic circular dichroism (MCD) techniques. Spectroscopic measurements during electrochemical, photochemical and chemical oxidation and reduction experiments have yielded high quality spectral data for the ring-oxidized radical cation and a range of ring-reduced species. As more data become available, the need for quantitative interpretation becomes more important. We describe in this review, progress towards understanding the optical spectrum of the phthalocyanines based on the spectral deconvolution analyses of absorption and magnetic circular dichroism data (MCD) and the use of ZINDO calculations to provide the theoretical model required to fully analyze these results.

Keywords: Metal phthalocyanines; Spectral band deconvolution analysis; ZINDO calculations

1. Introduction

Gouterman's four-orbital LCAO model has been widely used to describe the optical spectra of both metal porphyrin and metal phthalocyanine complexes [1–6]. Gouterman's model is based on a theoretical treatment that unites a 16 atom, 18 π-electron cyclic polyene model (Fig. 1) with a Huckel treatment that takes into account the structure of the porphyrin (P) or phthalocyanine (Pc) ring. The association of orbital angular momentum (OAM) with pairs of orbitals follows from the assignment of the molecular orbitals of the aromatic ring system in terms of the OAM associated with the complex wave functions of an ideal cyclic polyene in the sequence 0, ± 1, $\pm 2, \ldots, \pm 7$, 8 based on their nodal and anti-nodal patterns. The HOMO has an M_L value of ± 4 while the LUMO has an M_L value of ± 5. In this simple scheme there are four transitions between these two levels involving changes in orbital angular momentum of $\Delta M_L = \pm 1$ and ± 9 (Fig. 2) referred to as the B and Q transitions, respectively. Despite the obvious simplicity of this model, it provides a remarkably good description of the experimental spectral data of main group MP(−2) [7] complexes where the LUMO and HOMO levels essentially retain their degeneracy [1–6].

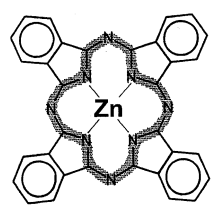

Fig. 1. Molecular structure of ZnPc(−2) showing the path of the 16-atom cyclic polyene ring used as the basis for the four-orbital LCAO calculations of Gouterman [1].

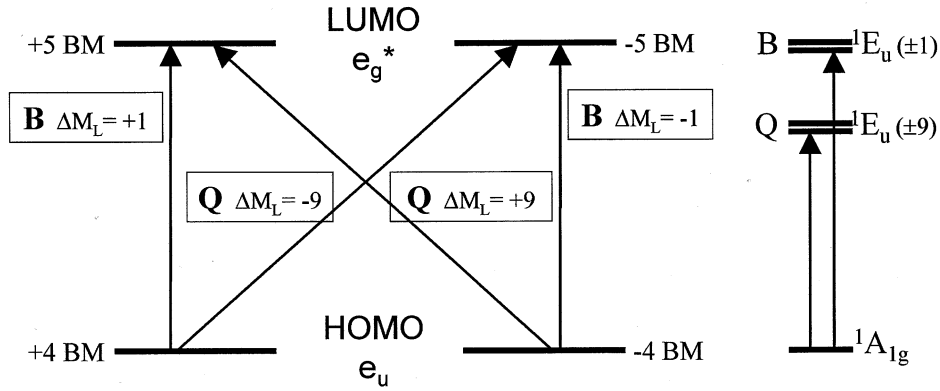

Fig. 2. The origin of the Q and B bands in Gouterman's four-orbital LCAO model. The doubly degenerate HOMO and LUMO exhibit ± 4 and ± 5 units of angular momentum, respectively. The four possible transitions result in the forbidden 'Q' band with $\Delta M_L = 9\beta$ and the allowed 'B' band with $\Delta M_L = 1\beta$. The two bands are readily recognized in the absorption and MCD spectra of metalloporphyrins with an intense B band near 400 nm with a weak MCD A term, and a very weak Q absorption band near 550 nm that exhibits an intense MCD A term [1].

The addition of the aza-linkages and peripheral fused benzene rings to form MPc(−2) breaks the accidental degeneracy of the HOMO level significantly so that the $1a_{1u}$ and $1a_{2u}$ orbitals become widely separated, resulting in the observation of the Q band near 670 nm and the B band set near 300 nm (Figs. 3 and 4). This results in reduced mixing between the Q and B excited states so that the forbidden and very weak Q band of the porphyrins gains significant intensity in the case of MPc complexes and is observed as an intense band near 670 nm [1]. The HOMO and LUMO orbitals of MPc complexes continue to closely resemble those of the 16-atom polyene. However, significantly, new MOs located primarily on the peripheral portions of the π-system of the Pc ring have a major influence on the spectral properties. Because of the influence of configuration interaction, only the $1a_{1u} \rightarrow 1e_g^*$ electronic transition that is responsible for the Q band, therefore, closely follows the predictions of the 4-orbital model. Electrochemical studies have shown that up to four electrons can be reversibly added to, or up to two reversibly removed from, the π-system of the phthalocyanine dianion ring. The optical spectra of ring reduced and ring-oxidized species provides information that is not available from the spectrum of the neutral species alone. Fig. 4 shows spectra for typical main group MPc species; the one-electron oxidized $[MgPc(-1)]^+$, the neutral ZnPc(−2), the one-electron ring-reduced $[ZnPc(-3)]^-$ and the two-electron ring-reduced $[ZnPc(-4)]^{2-}$ species. We have used Gouterman's model of the electronic structure as the theoretical framework within which to assign specific $\pi \rightarrow \pi^*$ transitions in MPc(−2) complexes and their anion and cation radicals, basing our assignment on spectral deconvolution studies of the UV–vis absorption and magnetic circular dichroism (MCD) spectral data [8–21] using the SIMPFIT program [12,22,23] and MO calculations obtained from the ZINDO program [24].

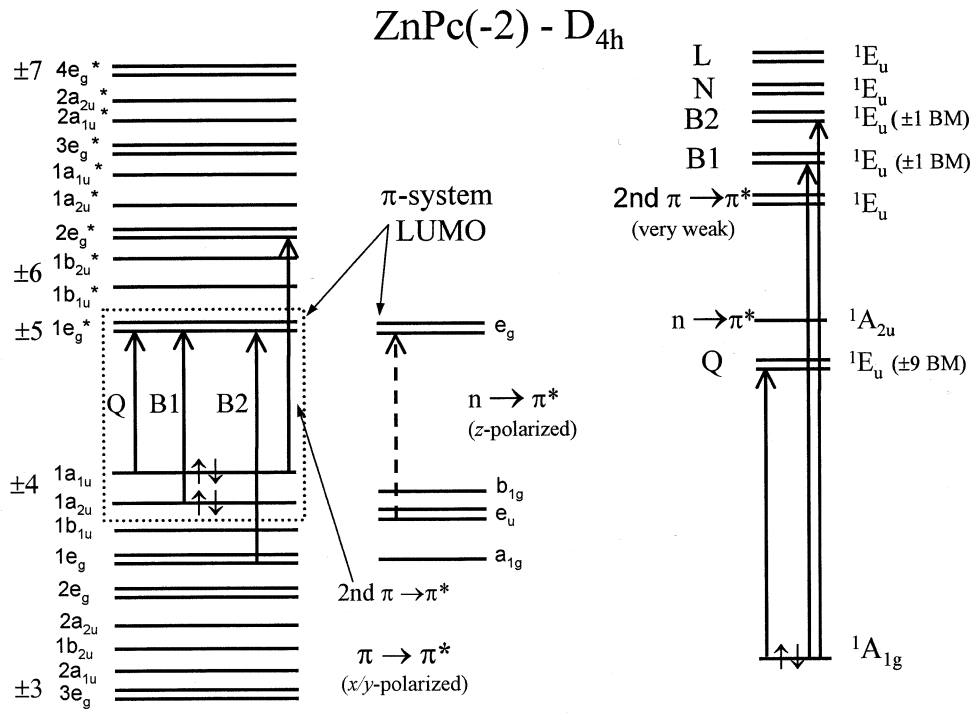

Fig. 3. Molecular orbital diagram of ZnPc(− 2) showing the transitions that are predicted to give rise to absorption bands in the 280–1000 nm range of the optical spectrum. The orbital ordering is based on current ZINDO calculations and spectral deconvolution studies [35], however, it follows closely the ordering first proposed by Gouterman and coworkers [4]. The dotted line indicates the four-orbitals referred to in Fig. 2 that are based on Gouterman's original four-orbital LCAO model [1]. Interspersed with the π MOs of the inner perimeter cyclic polyene ring are MOs that are associated primarily with the peripheral portions of the extended π-system (Table 5). The orbitals on the right of the main $\pi \rightarrow \pi^*$ set are the four aza-nitrogen lone pair MOs. Transitions that give rise to x/y-polarized bands are represented with solid lines. Dashed lines are used for z-polarized transitions that are predicted to lie in the Q band region. On the right hand side we show the states calculated to exhibit significant absorption intensity in the 250–1000 nm region, with the state symmetry for a D_{4h} molecular symmetry. The second $\pi \rightarrow \pi^*$ transition is observed as a very weak doubly degenerate band in the spectra of main group MPc(− 2) complexes.

Fig. 4. Typical room temperature absorption and MCD spectra of ring-oxidized $[MPc(-1)]^+$, neutral MPc(− 2), and the ring reduced $[MPc(-3)]^-$ and $[MPc(-4)]^{2-}$ species. The spectra were recorded on solutions of monomeric $[MgPc(-1)]^+$ in CH_2Cl_2 [19], ZnPc(− 2) in dimethyl formamide (DMF), $[ZnPc(-3)]^-$ in DMF–hydrazine hydrate [16] and $[ZnPc(-4)]^{2-}$ during the in situ spectroelectrochemical reduction of ZnPc(− 2) in a DMF/piperidine (5:1) solvent mixture with 0.1 M tetrapropylammonium perchlorate as the supporting electrolyte [35]. None of the MCD bands observed for $[ZnPc(-3)]^-$ can be fitted with A terms such as that seen for the Q band of ZnPc(− 2) at 670 nm. Reproduced with permission from Ref. [73].

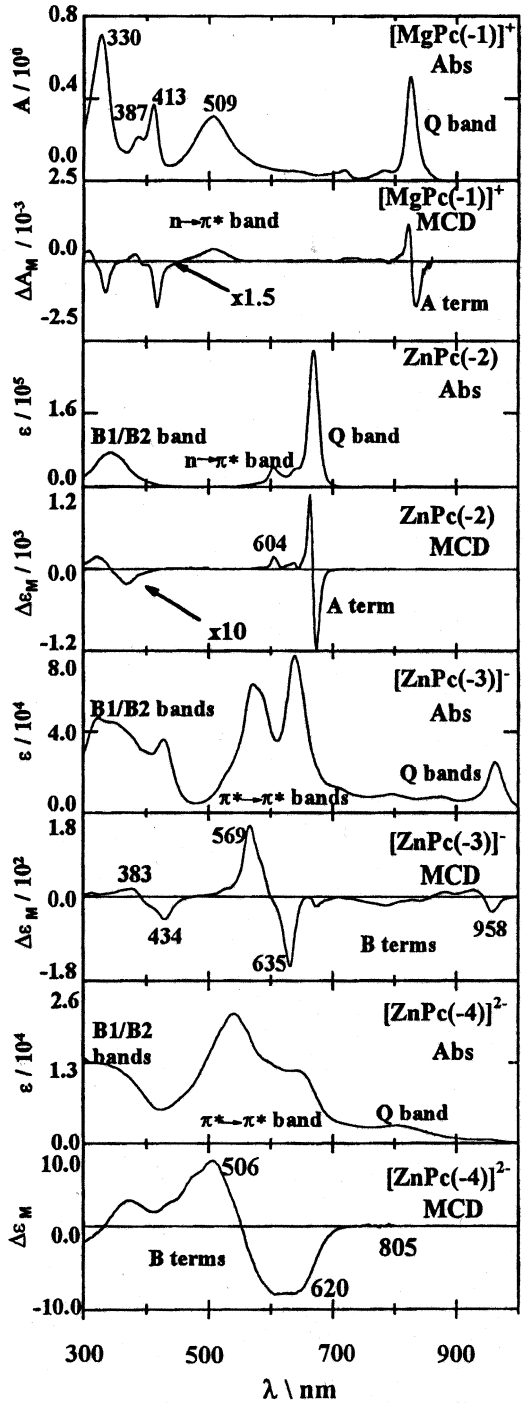
[MgPc(-1)]+
Abs
330
387
413
509
Q band
A / 10⁰
[MgPc(-1)]+
MCD
n→π* band
x1.5
A term
ΔA_M / 10⁻³
ZnPc(-2)
Abs
B1/B2 band
n→π* band
Q band
ε / 10⁵
ZnPc(-2)
MCD
604
x10
A term
Δε_M / 10³
[ZnPc(-3)]-
Abs
B1/B2 bands
π*→π* bands
Q bands
ε / 10⁴
[ZnPc(-3)]-
MCD
569
383
434
635
B terms
958
Δε_M / 10²
[ZnPc(-4)]2-
Abs
B1/B2 bands
π*→π* band
Q band
ε / 10⁴
[ZnPc(-4)]2-
MCD
506
B terms
620
805
Δε_M
300
500
700
900
λ \ nm

Fig. 4.

2. Techniques

2.1. Magnetic circular dichroism spectroscopy

The bands in the MCD spectrum [25,26] arise from the same transitions as those in the absorption spectrum but the band morphologies are significantly different as the applied external magnetic field has a significant impact on the orbital and spin degeneracies of electronic states. Both the orbital and spin angular moments have associated magnetic moments that can couple with an applied field leading to a splitting into $2J+1$ components. The intensity mechanism for MCD spectroscopy depends upon coupling of the ground and excited states through both the electric and magnetic dipole moments. MCD spectroscopy makes use of the Faraday magnet arrangement in which the applied field is parallel to the incident light. The specificity of the MCD technique arises from three highly characteristic spectral features known as the Faraday A, B and C terms (Fig. 5). The derivative-shaped

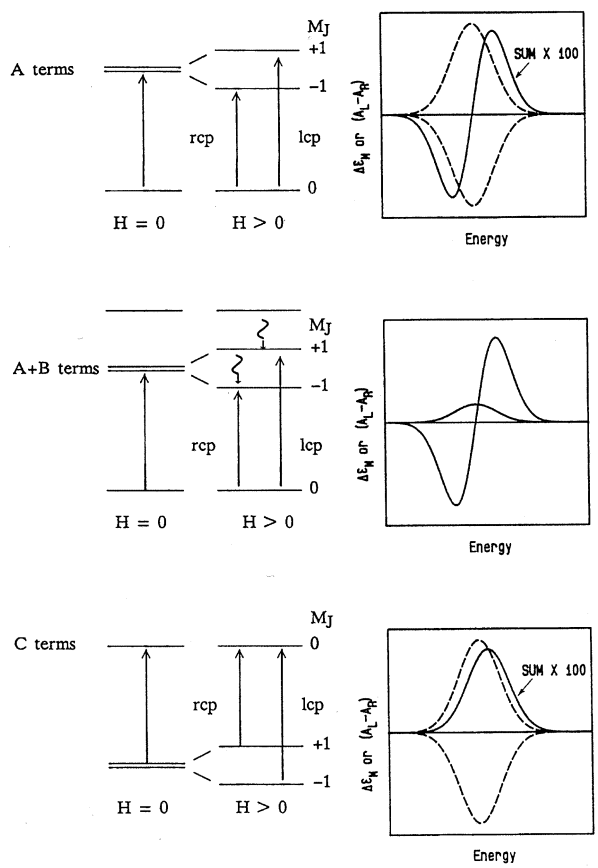

Fig. 5. Origin of the A, B and C Faraday terms observed in MCD spectra. The dashed curves represent the absorbance of left and right circularly polarized light (l/rcp).

Faraday A term is temperature independent and identifies degenerate excited states, while the normally Gaussian-shaped C term is highly temperature dependent and identifies an orbitally degenerate ground state. Gaussian-shaped, temperature independent B terms arise from mixing between closely related states linked by a magnetic dipole transition moment and can be either positive or negative. Complexes with symmetry lower than D_{4h} give rise exclusively to B terms. Michl [27,28] has demonstrated that when the symmetry is reduced below D_{4h}, the derivative-shaped x/y-polarized A terms are replaced by intense, coupled pairs of oppositely signed, x- and y-polarized Gaussian-shaped B terms. MCD spectral data for a variety of MPc complexes that adopt both highly symmetric and asymmetric structures indicate that in many cases, accidental degeneracy of the split states results in the observation of A term-like features.

2.2. Spectral band deconvolution analysis

Band deconvolution analyses of overlapping spectral bands tend to be greeted with skepticism. Since there can often be an unlimited number of potential fits when Gaussian-shaped bands are used to deconvolute a highly overlapping spectral envelope, it is difficult to justify any particular combination. The SIMPFIT program was designed to overcome this problem by carrying out the simultaneous spectral deconvolution of MCD and UV–vis absorption spectral data sets recorded on the same solution. The approach used in the SIMPFIT program rests on the fact that under the rigid shift assumption, it can be assumed that the application of a magnetic field will make no difference to the spectral band shape function [26,27]. The basic band parameters should therefore be the same in both spectra. The requirement that two spectra that arise from different selection rules be fitted with the same set of band parameters removes much of the ambiguity that is normally associated with band deconvolution analyses. The second spectral data set will eliminate most of the false minima encountered during the analysis of a single spectrum using iterative search techniques based on complex mathematical algorithms. To deconvolute overlapping spectral bands, it is necessary to determine the band shape, bandwidth and the band center of each band by optimizing their values to obtain the best possible agreement between the calculated and experimental spectral data through successive iterations. The band intensities are not a variable within the band fitting process since they have to be calculated for any given set of values of the three iteration variables [12,22,23]. To simplify the iteration process, the band shape parameter has also been eliminated as a variable in the SIMPFIT program through the use of a fixed band shape. The bands are normally assumed to be Gaussian curves as will be the case whenever the Born Oppenheimer and Frank Condon approximations can be made [12,22,23]. Although introducing a variable Lorentzian component for each band as a third parameter could in some instances result in a slightly better agreement with the experimental data, this would potentially introduce a 'fudge factor' into the band deconvolution analysis which we feel should be avoided.

SIMPFIT uses algorithms that improve the agreement between the calculated and experimental spectral data in a nonlinear manner to find the minimum in the χ^2-values on the response surface generated by all the possible sets of parameter values. A number of different mathematical algorithms have been developed which use different strategies to seek the minimum χ^2-value using the smallest possible number of iterations to derive the optimum fit [29]. The gradient-search method involves incrementing all the parameters simultaneously and then following the direction of maximum change in the response surface. This algorithm is useful for approaching the minimum from far away but has the drawback that it does not converge rapidly near the minimum. Another algorithm known as the expansion method gets around this problem by fitting an approximate analytical function to the response surface so that least-squares fitting methods can be used to locate the minimum. This technique cannot be relied upon to approach the minimum from outside the region in which the response surface resembles the approximate analytical function. The SIMPFIT program uses the Marquardt method for fitting absorption data [29] since this technique is based on introducing the approximate analytical function of the expansion method progressively into the gradient-search algorithm as the χ^2 of the fit is optimized.

The Marquardt method can usually be applied successfully to the absorption spectrum, since application of the expansion method is relatively straightforward if all the spectral bands have a fixed Gaussian-shape. In the case of MCD spectroscopy, however, the Faraday A term band shape function in the spectra of high symmetry molecules takes the form of a first derivative of the Gaussian band shape. The fact that the A and B terms have different band shapes and can be either positive or negative in sign within the MCD spectral envelope makes the fitting of an approximate analytical function to the response surface impossible in most instances. The SIMPFIT program therefore contains two different simplex algorithms that can be used for optimizing MCD spectral fits. The simplex iteration method was first proposed in its current form by Spendley et al. in 1962 [30]. A modified version referred to, as the Modified Simplex Method (MSM) was the first to find significant practical use [31]. A simplex is a geometrical form on a response surface in n dimensions and consists of $n+1$ vertices that are not all in the same $n-1$ dimensions. Each dimension corresponds to one of the parameters that are to be modified by the optimization procedure.

In the so-called basic simplex method (BSM) of Spendley et al. [30] after evaluation of the response at each point (see below) the vertex, which gives the least desirable response, W, is discarded and a new point, N, is produced by reflecting through the centroid of the opposite hyperface. The response at the new vertex is then compared to the remaining responses, and reflecting through the centroid of the appropriate hyperface produces another vertex. The process then continues until the variance in response at all $n+1$ vertices is below a preset value. In Nelder and Mead's [31] Modified Simplex Method (MSM), the method is initially the same as the BSM with $\alpha = 1.0$. If the response at N is better than at all the other vertices then the value of α is increased to 2.0 and a so-called extension is made to point NE. If this expansion point is less favorable than B and M, it will be discarded and

point N will be used to generate the new simplex. Conversely, if the initial reflection produces a point N that is less desirable than B and M, a contraction will be made. A positive contraction ($\alpha = 0.5$) will be made when N is more favorable than W and a negative contraction ($\alpha = -0.5$) will be made when N is less favorable than W to produce points PC and NC, respectively. Routh et al. [32] proposed a further improvement to this technique that is referred to as the super modified simplex (SMS). Once the worst vertex W is calculated, a parabola is passed through points W, C and N and the optimum value of α is calculated to determine the position of the new vertex. The SMS method was further enhanced by Ryan et al. [33] to produce the weighted centroid method (WCM). Given that vertex B gives a better response than vertex M, the optimal vector in which to calculate the position of the new vertex is probably closer to WB than WM. The position of the centroid C through which the parabola is generated is weighted to reflect this. The SIMPFIT program gives the user the option of using either the SMS or WCM simplex iterations. One drawback of all simplex iterations is that they can become distorted when the angle $\angle$BWM between one vertex and two neighboring points becomes so slight that the simplex loses its ability to search in the direction of this vertex and becomes a 'degenerate simplex'. Degeneracy usually results in convergence at a false minimum. The problem of becoming trapped in a false minimum is also encountered when the nonlinear least-squares iteration is used for absorption spectral data [29]. By cycling between the absorption and MCD spectra, a response surface minimum can be found that provides a satisfactory fit for both spectral data sets. To reduce the ambiguity of the fitting process still further, the assumption is made that the minimum number of bands should always be used so that the removal of just one band will result in a fit that is clearly unacceptable.

The SIMPFIT program [12,22,23] is designed to greatly minimize the total iteration time by providing the tools required to easily construct an the initial estimate of the iteration parameters that is reasonably close to the true minimum in the response surface. The program has a band stripping function based on a routine that generates an estimate of the band parameters by placing a peak at the point of maximum intensity in the difference spectrum between the calculated and experimental absorption spectra. The bandwidth and intensity that will result in the lowest possible χ^2 are then calculated. A text box grid can be used to manually change the initial band fitting parameters as it is optimized by switching back and forth between the absorption and MCD spectral data to ensure that the initial parameters provide a reasonable fit to both spectra. The most recent SIMPFIT for Windows version of the program also allows the user to add the spectra of known impurities to the fitting process. These spectra are not included as a parameter within the actual iteration processes but are factored in whenever the deconvoluted band intensities are calculated [23]. Iteration times can be greatly reduced by only dealing with small portions of a spectrum at a time as the user can adjust a band weight function for the relative emphasis on each individual band during the optimization process. By giving bands in all but one portion of the spectrum no weight, only the bands in a selected portion of the spectrum are optimized. The number of parameters being adjusted by the algorithms is reduced along with the

complexity of the response surfaces over which the optimization routines must travel. This means that each optimization can be carried out on a time scale that allows the user to monitor its progress in real time.

The band fitting process used by SIMPFIT rests on the assumption that the same band parameters can be used to fit both spectra. In the case of ZnPc(− 2), however, the MCD Q band, is clearly sharper than the corresponding absorption band at room temperature (Fig. 6) [20]. The rigid shift approximation, the fundamental assumption on which the band fitting is based, clearly cannot be made in this instance as factors other than the natural radiative lifetimes are influencing the bandwidths so that they are no longer the same in the absorption and MCD spectra. It should be pointed out that a lot of valuable information can be obtained from studies of room temperature data of high symmetry molecules as the distinctive derivative-shaped A terms can easily be distinguished from the Gaussian-

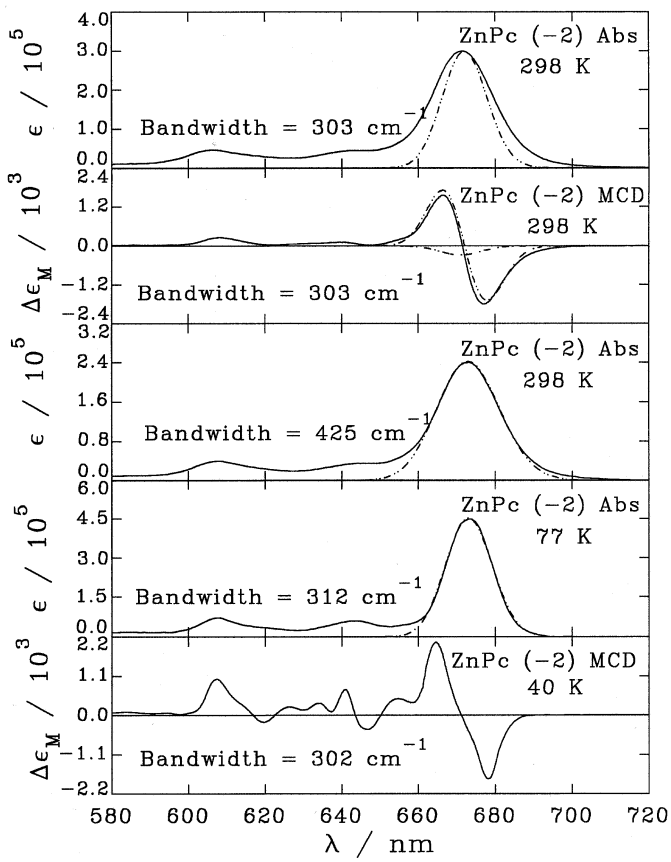

Fig. 6. The temperature dependence in the Q band region of the UV–vis absorption and MCD spectra of ZnPc(− 2) in liquid and vitrified solutions. The Gaussian curves illustrate the bandwidth discrepancy in the room temperature data. Reproduced with permission from Ref. [12].

shaped B terms. A discrepancy in the bandwidths makes meaningful band deconvolution impossible, however, when the MCD spectrum is dominated by extensively overlapping Gaussian B terms. Sutherland proposed that a zero-field splitting of the orbitally degenerate ^1E_u excited state could account for an analogous bandwidth discrepancy seen in the spectra of Zn and Mg coproporphyrin [34]. This discrepancy resulted in lower values for the orbital angular momentum calculated from the MCD experiment as the A_1/D_o parameter compared to those obtained from the Zeeman splitting of the separate absorption of left and right circularly polarized light. Sutherland [34] concluded that the Jahn–Teller splitting seen in the Shpol'skii spectra of metalloporphyrins is too minor to account for the large discrepancy seen in the spectral bandwidths. The interaction between the ring and the surrounding solvent molecules must therefore be responsible for the reduction in the symmetry of the excited state. The great multiplicity of possible solvation environments leads to a spread in the energy of the main transitions in the room temperature absorption spectrum. Solvation environments, which lead to a significant reduction in the overall symmetry, will quench the angular momentum of the excited states in the wings of the room temperature MCD envelope and result in a sharper MCD band and a concomitant reduction in the measured A_1/D_o value.

The Q_{00} band of ZnPc(-2) shows significant band sharpening when the solution is cooled from 298 to 210 K [20]. As the temperature is lowered, the higher energy solvation environments are partially depopulated and as a result, the absorption bands of ZnPc(-2) sharpen and intensify. On vitrification a 'freezing out' of the higher-energy solvation environments occurs and there is no temperature dependence in the Q_{00} band between 77 and 180 K. in the case of ZnPc(-2), the Q_{00} absorption band is significantly sharper and more intense than that measured in the same solution at room temperature (Fig. 6). The Q_{00} absorption band is almost perfectly Gaussian in shape at 77 K, while the corresponding band at 298 K cannot be fitted with a single Gaussian curve. The 77 K absorption bandwidth is in close agreement with the 298 K MCD bandwidth. The MCD spectrum is clearly also affected by the 'freezing out' of the higher-energy solvation environments but the peak to trough separation of the Q_{00} band does not appear to show any significant overall band sharpening. It is, therefore, possible to fit the absorption and MCD spectra recorded at cryogenic temperatures under the rigid shift assumption.

2.3. INDO calculations

In order to make full use of spectral band deconvolution data there usually needs to be a theoretical MO model to test the experimental spectral results against. In recent years we have used the ZINDO program in the software package of the CAChe workstation [24] to obtain calculated spectra for $[MPc(-(2+n))]^{n-}$ ($n = -1 \rightarrow 2$) species (Tables 1–4) [35]. The structures were refined using a modified MM2 force field calculation in the MECHANICS program of the CAChe system [36] and then optimized at the restricted Hartree–Fock self-consistent field (SCF) level [37] in the case of the diamagnetic species and at the restricted open-shell Hartree–

Table 1
Calculated electronic excitation spectrum of $[ZnPc(-1)]^+$

# [a]	Symmetry [b]	Calculated [c]	Observed [d]	Wave function [e] =	Assignment [f]
1	$^2A_{1u}$				Ground state
2, 3	$^2E_{gx}$	10.4 (0.237)	12.1	$-0.961\|1e_g^* \leftarrow 1a_{1u}\rangle + 0.131\|1e_g^* \leftarrow 1a_{2u}\rangle^A + \ldots$	Q
11, 12	$^2E_{gx}$	25.9 (0.109)	24.2	$-0.730\|1a_{1u} \leftarrow 2e_g\rangle + 0.295\|2e_g^* \leftarrow 1a_{1u}\rangle - 0.289\|1e_g^* \leftarrow 2b_{2u}\rangle^B + 0.204\|1e_g^* \leftarrow 1a_{2u}\rangle^B + \ldots$	$\pi \rightarrow \pi$
14, 18	$^2E_{gx}$	28.4 (0.077)	25.8	$0.662\|2e_g^* \leftarrow 1a_{1u}\rangle - 0.288\|1a_{1u} \leftarrow 1e_g\rangle + 0.273\|2e_g^* \leftarrow 2b_{1u}\rangle^B - 0.248\|1a_{2u}^* \leftarrow 2e_g\rangle^B - 0.231\|1b_{1u}^* \leftarrow 2e_g\rangle^B + 0.228\|1a_{1u} \leftarrow 2e_g\rangle + \ldots$	Second $\pi \rightarrow \pi^*$
19, 20	$^2E_{gx}$	30.6 (0.237)	30.3	$-0.506\|1e_g^* \leftarrow 1a_{2u}\rangle^B - 0.439\|1e_g^* \leftarrow 1a_{2u}\rangle^A - 0.364\|1a_{1u} \leftarrow 3e_g\rangle + 0.279\|1e_g^* \leftarrow 1a_{2u}\rangle^B + 0.202\|2e_g^* \leftarrow 1a_{1u}\rangle + \ldots$	B1
26, 27	$^2E_{gx}$	33.5 (0.085)	31.7	$-0.611\|1e_g^* \leftarrow 1b_{1u}\rangle^A - 0.320\|1e_g^* \leftarrow 1b_{1u}\rangle^B - 0.349\|1e_g^* \leftarrow 2a_{2u}\rangle^A - 0.206\|1e_g^* \leftarrow 2a_{2u}\rangle^B + \ldots$	B2
28, 31	$^2E_{gx}$	34.7 (0.840)	36.1	$0.753\|3e_g^* \leftarrow 1a_{1u}\rangle - 0.347\|2e_g^* \leftarrow 1a_{1u}\rangle - 0.292\|1e_g^* \leftarrow 1a_{2u}\rangle^A + \ldots$	N
35	$^2A_{2g}$	36.1 (0.015)	19.6	$0.492\|1e_g^* \leftarrow e_u^N\rangle^A + 0.354\|1e_g^* \leftarrow e_u^N\rangle^B - 0.359\|1b_{2u}^* \leftarrow b_{1g}^N\rangle^A + 0.299\|1b_{2u}^* \leftarrow b_{1g}^N\rangle^B + \ldots$	$n \rightarrow \pi^*$

[a] The number of the state assigned in terms of ascending energy in the ZINDO calculation. Only states which result from allowed electronic transitions with a non-zero oscillator strength are included in the table.

[b] The symmetry of the state under D_{4h} symmetry.

[c] The calculated band energies (10^3 cm^{-1}) and oscillator strengths in parenthesis.

[d] Observed band energies (10^3 cm^{-1}) for $[MPc(-1)]^+$ (M = Mg, Zn) from the data of Nyokong et al. [8] and Ough et al. [10].

[e] The calculated wave functions based on the eigenvectors produced by the configuration interaction calculation of the ZINDO program. A and B refer to separate spin-allowed excited state configurations associated with one-electron transitions linking the same orbitals. N denotes orbitals associated with the aza-nitrogen lone pair orbitals. The orbital energies of the π-system are shown in Table 5 [24].

[f] The assignment is described in the text.

Table 2
Calculated electronic excitation spectrum of ZnPc(−2)

# [a]	Symmetry [b]	Calculated [c]	Observed [d]	Wave function [e] =	Assignment [f]
1	$^1A_{1g}$				Ground state
2, 3	$^1E_{ux}$	14.8 (0.903)	14.8	$-0.950\|1e_g^* \leftarrow 1a_{1u}\rangle + 0.260\|1e_g^* \leftarrow 1a_{2u}\rangle + \ldots$	Q
6, 7	$^1E_{ux}$	30.0 (0.023)		$-0.978\|2e_g^* \leftarrow 1a_{1u}\rangle - 0.073\|4e_g^* \leftarrow 1a_{1u}\rangle + \ldots$	Second $\pi \rightarrow \pi^*$
13	$^1A_{2u}$	34.1 (0.032)	16.5	$0.561\|1e_g^* \leftarrow e_u^N\rangle - 0.472\|1b_{2u}^* \leftarrow b_{1g}^N\rangle + \ldots$	$n \rightarrow \pi^*$
14, 15	$^1E_{ux}$	34.3 (0.428)	25.5	$0.808\|1e_g^* \leftarrow 1b_{1u}\rangle - 0.255\|1b_{2u}^* \leftarrow 1e_g\rangle - 0.221\|1e_g^* \leftarrow 1a_{2u}\rangle + \ldots$	B1
16, 17	$^1E_{ux}$	34.7 (2.233)	29.9	$-0.815\|1e_g^* \leftarrow 1a_{2u}\rangle - 0.348\|3e_g^* \leftarrow 1a_{1u}\rangle - 0.252\|1e_g^* \leftarrow 1b_{1u}\rangle + 0.228\|1e_g^* \leftarrow 1a_{1u}\rangle + \ldots$	B2
21, 22	$^1E_{ux}$	36.5 (0.330)	33.6	$-0.574\|3e_g^* \leftarrow 1a_{1u}\rangle + 0.371\|1e_g^* \leftarrow 1a_{2u}\rangle - 0.259\|1b_{1u}^* \leftarrow 1e_g\rangle - 0.251\|2e_g^* \leftarrow 1b_{2u}\rangle - 0.222\|2e_g^* \leftarrow 1b_{1u}\rangle + \ldots$	N
29, 31	$^1E_{ux}$	39.0 (0.014)	36.2	$-0.635\|3e_g^* \leftarrow 1a_{1u}\rangle - 0.593\|1e_g^* \leftarrow 2b_{2u}\rangle + 0.278\|1e_g^* \leftarrow 2a_{1u}\rangle + 0.216\|1b_{2u} \leftarrow 2e_g^*\rangle + \ldots$	L
34, 35	$^1E_{ux}$	41.1 (0.019)	40.7	$-0.744\|1e_g^* \leftarrow 2a_{2u}\rangle 0.451\|1e_g^* \leftarrow 1b_{1u}\rangle - 0.293\|1e_g^* \leftarrow 1b_{2u}\rangle + 0.255\|3e_g^* \leftarrow 1a_{1u}\rangle + \ldots$	C

[a] The number of the state assigned in terms of ascending energy in the ZINDO calculation. Only states that result from allowed electronic transitions with a non-zero oscillator strength are included in the table.

[b] The symmetry of the state under D_{4h} symmetry.

[c] The calculated band energies (10^3 cm^{-1}) and oscillator strengths in parenthesis.

[d] Observed energies (10^3 cm^{-1}) from the data of Nyokong et al. [17].

[e] The calculated wave functions based on the eigenvectors produced by the configuration interaction calculation of the ZINDO program. N denotes orbitals associated with the aza-nitrogen lone pair orbitals. The orbital energies are shown in Table 5 [24].

[f] The assignment is described in the text.

Table 3
Calculated electronic excitation spectrum of $[ZnPc(-3)]^-$

# [a]	Symmetry [b]	Calculated [c]	Observed [d]	Wave function [e] =	Assignment [f]
1	$^2A_2$				Ground state
3	$^2A_2$	8.87 (0.097)	10.4	$0.842\|1a_2^* \leftarrow 1a_2\rangle + 0.370\|2a_2^* \leftarrow 2a_2\rangle - 0.281\|2a_2^* \leftarrow 1a_2\rangle^B + \ldots$	Q_z
4	$^2B_2$	10.4 (0.069)	10.8	$-0.683\|1b_2^* \leftarrow 1a_2\rangle^B + 0.438\|1b_2^* \leftarrow 1a_2\rangle^A - 0.435\|2b_2^* \leftarrow 2a_2^*\rangle + 0.138\|4b_2^* \leftarrow 1a_2\rangle^B + \ldots$	Q_x
5	$^2A_2$	16.6 (0.594)	15.7	$0.797\|2a_2^* \leftarrow 1a_2^*\rangle - 0.356\|1a_2^* \leftarrow 1a_2\rangle + 0.238\|1b_2^* \leftarrow 1b_2\rangle + 0.156\|3a_2^* \leftarrow 1a_2\rangle^B - 0.146\|4a_2^* \leftarrow 1a_2^*\rangle + \ldots$	$\pi^* \rightarrow \pi_z^*$
6	$^2B_2$	17.0 (0.292)	11.4	$-0.665\|3b_2^* \leftarrow 1a_2^*\rangle - 0.423\|2b_2^* \leftarrow 1a_2^*\rangle - 0.380\|1b_2^* \leftarrow 1a_2\rangle^A + 0.148\|1b_2^* \leftarrow 1a_2\rangle^B - 0.195\|3b_2^* \leftarrow 1a_2\rangle^B - 0.150\|2b_2^* \leftarrow 1a_2\rangle^B + \ldots$	$\pi^* \rightarrow \pi_x^*$
7	$^2B_2$	18.9 (0.469)	17.5	$-0.508\|1b_2^* \leftarrow 1a_2\rangle^A + 0.434\|4b_2^* \leftarrow 1a_2\rangle^B - 0.448\|4b_2^* \leftarrow 1a_2^*\rangle + 0.257\|3b_2^* \leftarrow 1a_2^*\rangle - 0.235\|2b_2^* \leftarrow 1a_2^*\rangle + 0.209\|2b_2^* \leftarrow 1a_2\rangle^B + \ldots$	Q_x/second $\pi^* \rightarrow \pi_x^*$
8	$^2B_2$	21.5 (0.207)		$-0.419\|1b_2^* \leftarrow 1a_2\rangle^A - 0.325\|1b_2^* \leftarrow 1a_2\rangle^B - 0.420\|4b_2^* \leftarrow 1a_2\rangle^B - 0.420\|4b_2^* \leftarrow 1a_2^*\rangle + 0.298\|3b_2^* \leftarrow 1a_2^*\rangle 0.226\|6b_2^* \leftarrow 1a_2^*\rangle + \ldots$	Q_x/second $\pi^* \rightarrow \pi_x^*$
12	$^2B_2$	25.5 (0.012)		$0.668\|2b_2^* \leftarrow 1a_2\rangle^A - 0.456\|2b_2^* \leftarrow 1a_2\rangle^B - 0.221\|3b_2^* \leftarrow 1a_2\rangle^A + 0.266\|3b_2^* \leftarrow 1a_2\rangle^B + \ldots$	
13	$^2A_2$	25.6 (0.130)		$-0.564\|4a_2^* \leftarrow 1a_2^*\rangle - 0.512\|4a_2^* \leftarrow 1a_2\rangle^A - 0.361\|3a_2^* \leftarrow 1a_2^*\rangle - 0.200\|6a_2^* \leftarrow 1a_2^*\rangle + \ldots$	Second $\pi^* \rightarrow \pi_z^*$
14	$^2B_2$	26.0 (0.179)	23.0	$-0.631\|1a_2^* \leftarrow 3b_2\rangle + 0.380\|1a_2^* \leftarrow 2b_2\rangle + 0.366\|1a_2^* \leftarrow 1b_2\rangle + \ldots$	$B1/B2_x$
17	$^2B_2$	27.3 (0.124)	24.8	$0.631\|4b_2^* \leftarrow 1a_2\rangle^A - 0.216\|4b_2^* \leftarrow 1a_2\rangle^B + 0.314\|1a_2^* \leftarrow 1b_2\rangle + 0.305\|4b_2^* \leftarrow 1a_2^*\rangle - 0.252\|1a_2^* \leftarrow 2b_2\rangle - 0.212\|1a_2^* \leftarrow 1b_2\rangle + \ldots$	Second $\pi \rightarrow \pi_x^*$
18	$^2A_2$	27.6 (0.061)		$-0.429\|3a_2^* \leftarrow 1a_2\rangle^A + 0.305\|3a_2^* \leftarrow 1a_2\rangle^B + 0.351\|5a_2^* \leftarrow 1a_2\rangle^B - 0.234\|6a_2^* \leftarrow 1a_2\rangle^B + \ldots$	
19	$^2B_2$	28.3 (0.173)		$0.528\|4b_2^* \leftarrow 1a_2\rangle^A - 0.204\|4b_2^* \leftarrow 1a_2\rangle^B - 0.438\|1a_2^* \leftarrow 1b_2\rangle + 0.249\|2a_2^* \leftarrow 1b_2\rangle + 0.240\|1a_2^* \leftarrow 2b_2\rangle + \ldots$	Second $\pi \rightarrow \pi_x^*$
23	$^2B_2$	30.8 (0.486)		$-0.400\|3b_2^* \leftarrow 1a_2\rangle^A + 0.258\|3b_2^* \leftarrow 1a_2\rangle^B - 0.304\|2a_2^* \leftarrow 1a_2\rangle^A + 0.327\|1a_2^* \leftarrow 3b_2\rangle + 0.305\|1a_2^* \leftarrow 2b_2\rangle - 0.292\|1a_2^* \leftarrow 5b_2\rangle + 0.219\|1a_2^* \leftarrow 1b_2\rangle + \ldots$	$B1/B2_x$
24	$^2A_2$	31.2 (0.031)		$0.539\|2a_2^* \leftarrow 1a_2\rangle^B - 0.303\|5a_2^* \leftarrow 1a_2^*\rangle^B + 0.243\|1a_2^* \leftarrow 2a_2\rangle + 0.232\|3a_2^* \leftarrow 1a_2\rangle^A - 0.212\|5a_2^* \leftarrow 1a_2\rangle^B - 0.206\|4a_2^* \leftarrow 1a_2^*\rangle^B + \ldots$	

Table 3 (*Continued*)

# [a]	Symmetry [b]	Calculated [c]	Observed [d]	Wave function [e] =	Assignment [f]
25	$^2B_2$	31.9 (0.255)		$0.686\|3b_2^* \leftarrow 1a_2\rangle^A + 0.262\|1a_2^* \leftarrow 1b_2\rangle - 0.205\|6b_2^* \leftarrow 1a_2^*\rangle - 0.202\|5b_2^* \leftarrow 1a_2^*\rangle^B + \ldots$	$B1/B2_x$
26	$^2B_2$	32.0 (0.032)		$0.397\|1b_2^* \leftarrow 2b_2\rangle^B - 0.303\|2a_2^* \leftarrow 1a_2\rangle^B - 0.326\|2a_2^* \leftarrow 1a_2^*\rangle - 0.282\|4a_2^* \leftarrow 1a_2^*\rangle + 0.235\|3a_2^* \leftarrow 1a_2^*\rangle + 0.216\|5a_2^* \leftarrow 1b_2\rangle + 0.217\|3a_2^* \leftarrow 1a_2\rangle^A + 0.215\|1b_2^* \leftarrow 4b_2\rangle^B + 0.202\|1b_2^* \leftarrow 1b_2\rangle^B + \ldots$	
27	$^2B_2$	32.6 (0.141)		$0.293\|2b_2^* \leftarrow 1a_2\rangle^B + 0.175\|5b_2^* \leftarrow 1a_2\rangle^A + 0.245\|1a_2^* \leftarrow 1b_2\rangle - 0.263\|3b_2^* \leftarrow 1a_2\rangle + 0.255\|6b_2^* \leftarrow 1a_2\rangle - 0.259\|3a_2^* \leftarrow 4b_2\rangle^B - 0.223\|1b_2^* \leftarrow 3a_2\rangle^B + \ldots$	
28	$^2A_2$	32.7 (0.045)		$0.519\|1a_2^* \leftarrow 2a_2\rangle - 0.249\|6a_2^* \leftarrow 1a_2\rangle - 0.230\|3a_2^* \leftarrow 1a_2^*\rangle^A + 0.206\|4a_2^* \leftarrow 1a_2\rangle + 0.203\|1b_2^* \leftarrow 2b_2\rangle^B + \ldots$	
30	$^2A_2$	33.7 (0.023)		$0.408\|1b_2^* \leftarrow 2b_2\rangle^B - 0.336\|4b_2^* \leftarrow 2b_2\rangle^B - 0.252\|3a_2^* \leftarrow 2b_2^*\rangle^A + 0.207\|3a_2^* \leftarrow 1a_2\rangle^B + 0.225\|2a_2^* \leftarrow 1a_2\rangle^B + 0.210\|4b_2^* \leftarrow 1b_2\rangle^B + \ldots$	
31	$^2A_2$	34.0 (0.274)		$-0.578\|1b_2^* \leftarrow 1b_2\rangle^B + 0.187\|1b_2^* \leftarrow 2b_2\rangle^A - 0.265\|4b_2^* \leftarrow 2b_2\rangle^B + 0.222\|3a_2^* \leftarrow 1a_2\rangle^A - 0.219\|3a_2^* \leftarrow 1a_2\rangle^B - 0.222\|5a_2^* \leftarrow 1a_2\rangle^A + \ldots$	$B1/B2_z$
33	$^2B_1$	34.5 (0.013)		$-0.698\|1a_2^* \leftarrow 2b_1^N\rangle - 0.430\|1b_2^* \leftarrow 2a_1^N\rangle - 0.181\|1a_2^* \leftarrow 1b_1^N\rangle - 0.136\|6a_2^* \leftarrow 1b_1^N\rangle + \ldots$	$n \rightarrow \pi^*$
34	$^2A_2$	34.8 (0.115)		$0.370\|1a_2^* \leftarrow 3a_2\rangle + 0.338\|5a_2^* \leftarrow 1a_2\rangle^A - 0.132\|5a_2^* \leftarrow 1a_2\rangle^B + 0.272\|1b_2^* \leftarrow 1b_2\rangle^A - 0.171\|1b_2^* \leftarrow 1b_2\rangle^B - 0.282\|2a_2^* \leftarrow 1a_2\rangle^A + \ldots$	
36	$^2A_2$	35.1 (0.352)		$-0.473\|5a_2^* \leftarrow 1a_2\rangle^A + 0.227\|1b_2^* \leftarrow 1b_2\rangle^A + 0.291\|1b_2^* \leftarrow 2b_2\rangle^A - 0.159\|1b_2^* \leftarrow 2b_2\rangle^B + \ldots$	

[a] The number of the state assigned in terms of ascending energy in the ZINDO calculation. Only states that result from allowed electronic transitions with a calculated oscillator strength greater than 0.01 are included in the table.

[b] The symmetry of the state under C_{2v}(III) symmetry.

[c] The calculated band energies (10^3 cm^{-1}) and oscillator strengths in parenthesis.

[d] Observed band energies (10^3 cm^{-1}) from the data of Mack and Stillman [16].

[e] The calculated wave functions based on the eigenvectors produced by the configuration interaction calculation of the ZINDO program. A and B refer to separate spin-allowed excited state configurations associated with one-electron transitions linking the same orbitals. N denotes orbitals associated with the aza-nitrogen lone pair orbitals. The orbital energies are shown in Table 5 [24].

[f] The assignment is described in the text.

Table 4
Calculated electronic excitation spectrum of $[ZnPc(-4)]^{2-}$

# [a]	Symmetry [b]	Calculated [c]	Observed [d]	Wave function [e] =	Assignment [f]
1	^1A_g				Ground state
3	$^1B_{2u}$	17.9 (1.025)	16.1	$-0.983\|1a_u^* \leftarrow 1b_{2g}^*\rangle + \ldots$	$\pi^* \rightarrow \pi_y^*$
4	$^1B_{3u}$	18.9 (0.153)	19.7	$0.890\|1b_{1u}^* \leftarrow 1b_{2g}^*\rangle - 0.294\|2b_{1u}^* \leftarrow 1b_{2g}^*\rangle + \ldots$	$\pi^* \rightarrow \pi_x^*$
6	$^1B_{3u}$	20.8 (1.347)	11.6	$0.903\|1b_{3g}^* \leftarrow 1a_u\rangle + 0.331\|2b_{1u}^* \leftarrow 1b_{2g}^*\rangle + 0.163\|2b_{3g}^* \leftarrow 1a_u\rangle - 0.122\|1b_{1u}^* \leftarrow 1b_2^*\rangle + \ldots$	Q_x
8	$^1B_{3u}$	21.4 (0.174)		$0.785\|2b_{1u}^* \leftarrow 1b_{2g}^*\rangle + 0.408\|1b_{1u}^* \leftarrow 1b_{2g}^*\rangle + 0.298\|1b_{3g}^* \leftarrow 1a_u\rangle + 0.264\|2b_{3g}^* \leftarrow 1a_u\rangle + \ldots$	Second $\pi^* \rightarrow \pi_x^*$
11	$^1B_{2u}$	28.1 (0.435)		$0.792\|2a_u^* \leftarrow 1b_{2g}^*\rangle + 0.517\|2b_{2g}^* \leftarrow 1a_u\rangle + 0.203\|3b_{2g}^* \leftarrow 1a_u\rangle + \ldots$	Second $\pi^* \rightarrow \pi_y^*$
13	$^1B_{2u}$	29.5 (0.095)		$0.831\|2b_{2g}^* \leftarrow 1a_u\rangle - 0.488\|2a_u^* \leftarrow 1b_{2g}^*\rangle + \ldots$	Second $\pi \rightarrow \pi_y^*$
15	$^1B_{3u}$	33.1 (0.274)		$-0.730\|3b_{1u}^* \leftarrow 1b_{2g}^*\rangle - 0.566\|2b_{3g}^* \leftarrow 1a_u\rangle + 0.308\|2b_{1u}^* \leftarrow 1b_{2g}^*\rangle + \ldots$	Third $\pi^* \rightarrow \pi_x^*$
17	$^1B_{2u}$	34.3 (0.093)		$-0.777\|3a_u^* \leftarrow 1b_{2g}^*\rangle - 0.332\|1b_{3g}^* \leftarrow 2b_{1u}\rangle - 0.328\|3b_{2g}^* \leftarrow 1a_u\rangle + \ldots$	Third $\pi^* \rightarrow \pi_y^*$
18	$^1B_{1u}$	34.7 (0.024)		$0.699\|1b_{2g}^* \leftarrow 1b_{3u}^N\rangle + 0.544\|1a_u^* \leftarrow 1b_{1g}^N\rangle + \ldots$	$n \rightarrow \pi^*$
19	$^1B_{2u}$	35.0 (1.267)		$-0.855\|1b_{3g}^* \leftarrow 1b_{1u}\rangle - 0.226\|1a_u^* \leftarrow 1b_{2g}\rangle + \ldots$	$B1_y$
21	$^1B_{3u}$	35.5 (0.079)		$-0.698\|2b_{3g}^* \leftarrow 1a_u\rangle + 0.581\|3b_{1u}^* \leftarrow 1b_{2g}^*\rangle + 0.249\|3b_{3g}^* \leftarrow 1a_u\rangle + \ldots$	Second $\rightarrow \pi_x^*$

[a] The number of the state assigned in terms of ascending energy by the ZINDO calculation. Only states that result from allowed electronic transitions with a non-zero oscillator strength are included in the table.

[b] The symmetry of the state under D_{2h}(II) symmetry.

[c] The calculated band energies (10^3 cm^{-1}) and oscillator strengths in parenthesis.

[d] Observed band energies from the data reported in this paper.

[e] The calculated wave functions based on the eigenvectors produced by the configuration interaction calculation of the ZINDO program. N denotes orbitals associated with the aza-nitrogen lone pair orbitals. The orbital energies are shown in Table 5 [24].

[f] The assignment is described in the text.

Fock (ROHF) SCF level [38–43] in the case of the paramagnetic species using the ZINDO program in the CAChe software package [44–53]. These SCF optimizations were carried out at the intermediate neglect of differential overlap/1 [54] (INDO/1) level of approximation. The calculated energies of the π-system MOs in the -11 to 3 eV range of a $ZnC_8N_8H_8$ model complex comprising just the inner cyclic polyene ring of ZnPc referred to here as ZnCP, zinc tetraazaporphyrin (ZnTAP), and $[MPc(-(2+n))]^{n-}$ $(n=-1\rightarrow 2)$ species; Tables 1–4 are shown schematically in Table 5. The orbitals are ordered in terms of the distinctive nodal and anti-nodal patterns observed for ZnPc(-2) MOs that are found consistently over the range of complexes so that the one-electron transitions responsible for the bands in the ZINDO calculated spectra of each species can be compared.

3. Spectral band assignments using spectral band deconvolution: the MPc(-2) species

In 1973, Schaeffer et al. [4] proposed a band assignment scheme for MPc(-2) complexes based on five major $\pi\rightarrow\pi^*$ bands referred to as Q, B, N, L and C in terms of ascending energy observed at 660, 320, 275, 245 and 210 nm, respectively. The ground states of divalent, main group D_{4h} MPc(-2) complexes are $^1A_{1g}$, while the accessible $\pi\rightarrow\pi^*$ excited states are ^1E_u (x/y-polarized) (Fig. 3). The absorption spectra of ZnPc(-2) include an intense Q band (ε ca. 10^5) near 670 nm, followed by a series of vibrational components, Q_{vib}, and a broad envelope of overlapping bands in the 250–400 nm region (Figs. 7 and 8). Our spectral deconvolution studies [8–12,14,17–20,35] have indicated that there are two A terms of almost equal magnitude and bandwidth in the B region of the spectrum of MPc(-2) complexes (250–400 nm) as a result of the $1b_{1u}\rightarrow 1e_g^*$ one-electron transition mixing with the B transition of Gouterman's model. These bands can only be resolved clearly in the presence of certain axial ligands such as the cyanide ion. The band assignment sequence has therefore been modified to include separate B1 and B2 transitions superimposed in the 350 nm region [9] (Fig. 7).

Recent ZINDO calculations have indicated that the B1 and B2 bands seen in the spectrum of (CN^-)ZnPc(-2) [8,9] at 386 and 331 nm arise primarily from the $1a_{2u}\rightarrow 1e_g^*$ and $1b_{1u}\rightarrow 1e_g^*$ one-electron transitions. The $1b_{1u}$ orbital is not a factor in MP(-2) spectra as it is associated with the expansion of the π-system (Table 5). The N and L bands at 298 and 276 nm were found to have significant contributions from the $1a_{1u}\rightarrow 3e_g^*$ transition of the π-system (Table 2) while the C band at 246 nm is found to arise primarily from a $2a_{2u}\rightarrow 1e_g^*$ transition. Although the one-electron transitions associated with the higher energy bands has been modified somewhat from those of Schaeffer et al. [4] the Q, B1, B2, N, L and C band nomenclature [8–12,14,15,17–20] has been retained [35]. A new weaker $\pi\rightarrow\pi^*$ band has been identified slightly to the red of the B1/B2 spectral envelope. The ZINDO calculations indicated that the splitting of the $1a_{1u}$ and $1a_{2u}$ HOMOs of MPc(-2) is of sufficient magnitude for the $1a_{1u}\rightarrow 2e_g^*$ transition to sit at a lower energy than the $1a_{2u}\rightarrow 1e_g^*$ transition (Table 2 and Fig. 3). A very weak, derivative-shaped signal

Table 5
The calculated orbital energies and symmetries of ZnCP a complex comprising the inner cyclic polyene ring of ZnPc (ZnCP), zinc tetraazaporphyrin (ZnTAP), $[ZnPc(-1)]^{+}$, $ZnPc(-2)$, $[ZnPc(-3)]^{-}$ and $[ZnPc(-4)]^{2-}$. The rows are ordered according to the nodal and anti-nodal patterns that are observed for each complex relative to the high symmetry $ZnPc(-2)$ parent complex. The orbital angular momentum associated with the orbitals of the inner cyclic polyene is shown in the left hand column. The orbitals with the corresponding nodal and anti-nodal patterns are highlighted in bold. Italics are used to indicate degenerate orbitals under D_{4h} symmetry.

M_L	ZnCP		ZnTAP		$[ZnPc(-1)]^{+}$		$ZnPc(-2)$		$[ZnPc(-3)]^{-}$		$[ZnPc(-4)]^{2-}$	
	D_{4h}	E (eV)	D_{4h}	E (eV)	D_{4h}	E (eV)	D_{4h}	E (eV)	C_{2v}(III)	E (eV)	D_{2h}(II)	E (eV)
					$3b_{2u}^{*}$	1.162	$3b_{2u}^{*}$	3.844	$10b_{2}^{*}$	7.324	$5a_{u}^{*}$	9.387
					$5e_{g}^{*}$	1.126	$5e_{g}^{*}$	3.792	$9b_{2}^{*}$	*6.485*	$5b_{3g}^{*}$	*8.966*
						1.124		3.791	$9a_{2}^{*}$	*6.259*	$5b_{2g}^{*}$	*9.411*
					$2a_{1u}^{*}$	1.070	$2a_{1u}^{*}$	3.678	$8a_{2}^{*}$	6.140	$4a_{u}^{*}$	8.572
8	$\mathbf{1a_{2u}^{*}}$	**2.385**	$\mathbf{2a_{2u}^{*}}$	**2.961**	$\mathbf{2a_{2u}^{*}}$	**−0.016**	$\mathbf{2a_{2u}^{*}}$	**2.961**	$\mathbf{8b_{2}^{*}}$	**5.680**	$\mathbf{4b_{1u}^{*}}$	**8.672**
±7	$\boldsymbol{2e_{g}^{*}}$	***2.945***	$\boldsymbol{3e_{g}^{*}}$	***2.945***	$\boldsymbol{4e_{g}^{*}}$	***−0.003***	$\boldsymbol{4e_{g}^{*}}$	***2.945***	$\boldsymbol{7b_{2}^{*}}$	***5.579***	$\boldsymbol{4b_{3g}^{*}}$	***8.331***
		2.946		***2.946***		***−0.002***		***2.946***	$\boldsymbol{7a_{2}^{*}}$	***5.529***	$\boldsymbol{4b_{2g}^{*}}$	***8.311***
					$2b_{2u}^{*}$	−0.452	$2b_{2u}^{*}$	2.310	$6a_{2}^{*}$	4.770	$3b_{1u}^{*}$	7.577
					$2b_{1u}^{*}$	−0.851	$2b_{1u}^{*}$	2.066	$6b_{2}^{*}$	4.680	$3a_{u}^{*}$	7.448
			$2e_{g}^{*}$	*1.707*	$3e_{g}^{*}$	*−1.003*	$3e_{g}^{*}$	*1.677*	$5b_{2}^{*}$	*4.147*	$3b_{3g}^{*}$	*6.936*
				1.704		*−1.005*		*1.676*	$5a_{2}^{*}$	*4.155*	$3b_{2g}^{*}$	*6.656*
			$1a_{2u}^{*}$	2.310	$1a_{1u}^{*}$	−1.091	$1a_{1u}^{*}$	1.544	$4a_{2}^{*}$	3.995	$2a_{u}^{*}$	6.513
			$1a_{1u}^{*}$	1.975	$1a_{2u}^{*}$	−1.825	$1a_{2u}^{*}$	0.787	$3b_{2}^{*}$	3.284	$2b_{1u}^{*}$	6.027
					$2e_{g}^{*}$	*−1.893*	$2e_{g}^{*}$	*0.736*	$4b_{2}^{*}$	*3.317*	$2b_{3g}^{*}$	*6.008*
						−1.895		*0.734*	$3a_{2}^{*}$	*3.054*	$2b_{2g}^{*}$	*5.408*
±6	$\mathbf{1b_{2u}^{*}}$	**1.644**	$\mathbf{1b_{2u}^{*}}$	**1.180**	$\mathbf{1b_{2u}^{*}}$	**−2.441**	$\mathbf{1b_{2u}^{*}}$	**0.359**	$\mathbf{2b_{2}^{*}}$	**2.779**	$\mathbf{1b_{1u}^{*}}$	**5.275**
	$\mathbf{1b_{1u}^{*}}$	**0.763**	$\mathbf{1b_{1u}^{*}}$	**−0.266**	$\mathbf{1b_{1u}^{*}}$	**−2.626**	$\mathbf{1b_{1u}^{*}}$	**0.098**	$\mathbf{2a_{2}^{*}}$	**2.340**	$\mathbf{1a_{u}^{*}}$	**4.910**
±5	$\boldsymbol{1e_{g}^{*}}$	***−1.989***	$\boldsymbol{1e_{g}^{*}}$	***−1.843***	$\boldsymbol{1e_{g}^{*}}$	***−4.424***	$\boldsymbol{1e_{g}^{*}}$	***−1.495***	$\boldsymbol{1b_{2}^{*}}$	***1.434***	$\boldsymbol{1b_{3g}^{*}}$	***4.251***
		−1.987		***−1.842***		***−4.428***		***−1.493***	$\boldsymbol{1a_{2}^{*}}$	***−2.301***	$\boldsymbol{1b_{2g}^{*}}$	***0.434***

Table 5 (*Continued*)

M_L	ZnCP		ZnTAP		$[ZnPc(-1)]^+$		ZnPc(−2)		$[ZnPc(-3)]^-$		$[ZnPc(-4)]^{2-}$	
	D_{4h}	E (eV)	D_{4h}	E (eV)	D_{4h}	E (eV)	D_{4h}	E (eV)	C_{2v}(III)	E (eV)	D_{2h}(II)	E (eV)
±4	**$1a_{1u}$**	**−6.328**	**$1a_{1u}$**	**−6.264**	**$1a_{1u}$**	**−8.506**	**$1a_{1u}$**	**−5.534**	**$1a_2$**	**−3.029**	**$1a_u$**	**−0.714**
	$1a_{2u}$	**−8.431**	**$1a_{2u}$**	**−8.365**	**$1a_{2u}$**	**−11.102**	**$1a_{2u}$**	**−8.318**	**$1b_2$**	**−5.574**	**$1b_{1u}$**	**−2.815**
			$1b_{1u}$	−9.211	$1b_{1u}$	−11.455	$1b_{1u}$	−8.780	$3b_2$	−6.029	$2a_u$	−3.045
			$1e_g$	*−9.241*	*$1e_g$*	*−11.473*	*$1e_g$*	*−8.811*	*$2b_2$*	*−5.876*	*$1b_{3g}$*	*−2.884*
				−9.246		*−11.475*		*−8.813*	*$3a_2$*	*−6.245*	*$1b_{2g}$*	*−3.998*
					$2e_g$	*−11.575*	*$2e_g$*	*−9.021*	*$2a_2$*	*−6.218*	*$2b_{3g}$*	*−3.478*
						−11.576		*−9.021*	*$4b_2$*	*−6.591*	*$2b_{2g}$*	*−4.203*
					$2a_{2u}$	−11.661	$2a_{2u}$	−9.161	$4a_2$	−6.621	$2b_{1u}$	−4.070
			$1b_{2u}$	−9.765	$1b_{2u}$	−12.090	$1b_{2u}$	−9.297	$5b_2$	−6.632	$3b_{1u}$	
					$2a_{1u}$	−12.215	$2a_{1u}$	−9.711	$5a_2$	−7.208	$4a_u$	−4.829
±3	***$1e_g$***	***−10.390***	***$2e_g$***	***−10.399***	***$3e_g$***	***−13.413***	***$3e_g$***	***−10.695***	***$6b_2$***	***−7.802***	***$3b_{3g}$***	***−5.060***
	$1e_g$	***−10.392***		***−10.401***		***−13.416***		***−10.698***	***$6a_2$***	***−8.076***	***$3b_{2g}$***	***−5.582***
±2	**$1b_{2u}$**	**−12.730**	**$2b_{2u}$**	**−12.782**	**$2b_{2u}$**	**−14.927**	**$2b_{2u}$**	**−12.870**	**$7b_2$**	**−9.582**	**$5a_u$**	**−7.157**
	$1b_{1u}$	**−13.063**	**$2b_{1u}$**	**−13.670**	**$2b_{1u}$**	**−15.681**	**$2b_{1u}$**	**−12.275**	**$7a_2$**	**−9.986**	**$4b_{1u}$**	**−6.859**
					$4e_g$	*−15.697*	*$4e_g$*	*−13.088*	*$8b_2$*	*−10.827*	*$4b_{3g}$*	*−8.157*
						−15.699		*−13.089*	*$8a_2$*	*−10.619*	*$4b_{2g}$*	*−7.496*
					$3a_{2u}$	−15.876	$3a_{2u}$	−13.292	$9b_2$	−10.712	$5b_{1u}$	−8.121
					$3b_{2u}$	−17.854	$3b_{2u}$	−15.157	$10b_2$	−12.443	$6b_{1u}$	−9.789
±1	***$2e_g$***	***−14.898***	***$3e_g$***	***−15.040***	***$5e_g$***	***−18.878***	***$5e_g$***	***−16.085***	***$11b_2$***	***−13.118***	***$5b_{3g}$***	***−10.774***
		−14.898		***−15.046***		***−16.878***		***−16.086***	***$9a_2$***	***−13.393***	***$5b_{2g}$***	***−10.145***
0	**$2a_{2u}$**	**−16.256**	**$2a_{2u}$**	**−16.151**	**$4a_{2u}$**	**−19.946**	**$4a_{2u}$**	**−17.101**	**$12b_2$**	**−14.211**	**$7b_{1u}$**	**−11.254**

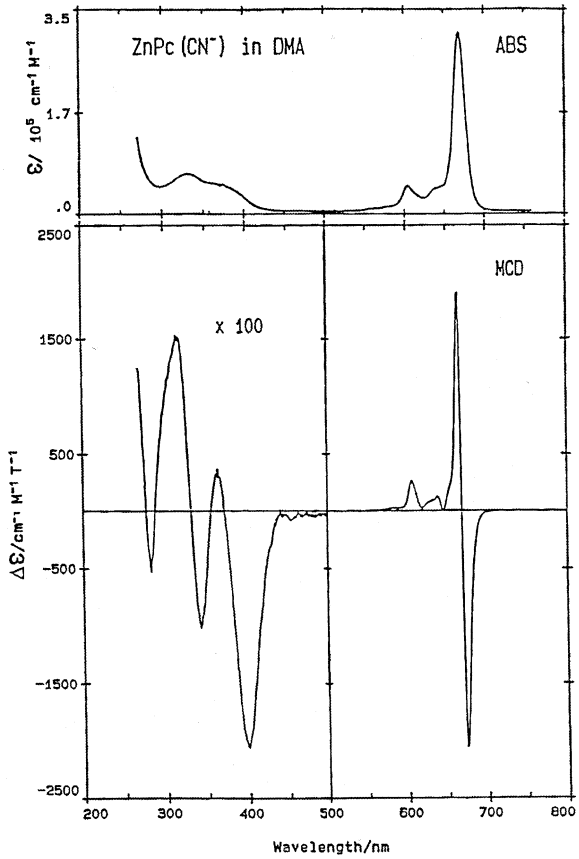

Fig. 7. Room temperature absorption and MCD spectral data for $(CN^-)ZnPc(-2)$ in dimethyl acetamide. The three main bands that characterize the optical spectra of all main group $MPc(-2)$ complexes are readily apparent, namely, the B1/B2 envelope between 300 and 425 nm and the Q band at 670 nm. Each of the absorption bands is associated with a positive A term that identifies the doubly degenerate excited state and the non-degenerate ground state of the associated electronic transitions. Reproduced with permission from Ref. [8].

seen in an MCD spectrum reported previously for $MgPc(-2)$ [9,15,18] at around 435 nm is assigned as an A term associated with this transition. This second $\pi \rightarrow \pi^*$ transition is not predicted to have significant intensity. The $2e_g^*$ MO is associated with π-system expansion (Table 5) and there is almost no mixing with the excited state associated with the allowed B1 transition of the inner perimeter 16 atom 18 π-electron cyclic polyene.

Fig. 8 shows the deconvolution results for the Q and Q_{vib} regions for $(CN^-)ZnPc(-2)$ [20] while Fig. 9 shows the trend in calculated bandwidths (plotted on a scale where the sign of the B term is either negative or positive) of the bands in the Q region as a function of band center energy. Our recent spectral deconvolution analysis of the UV–vis and MCD spectra of $ZnPc(-2)$ Q spectral

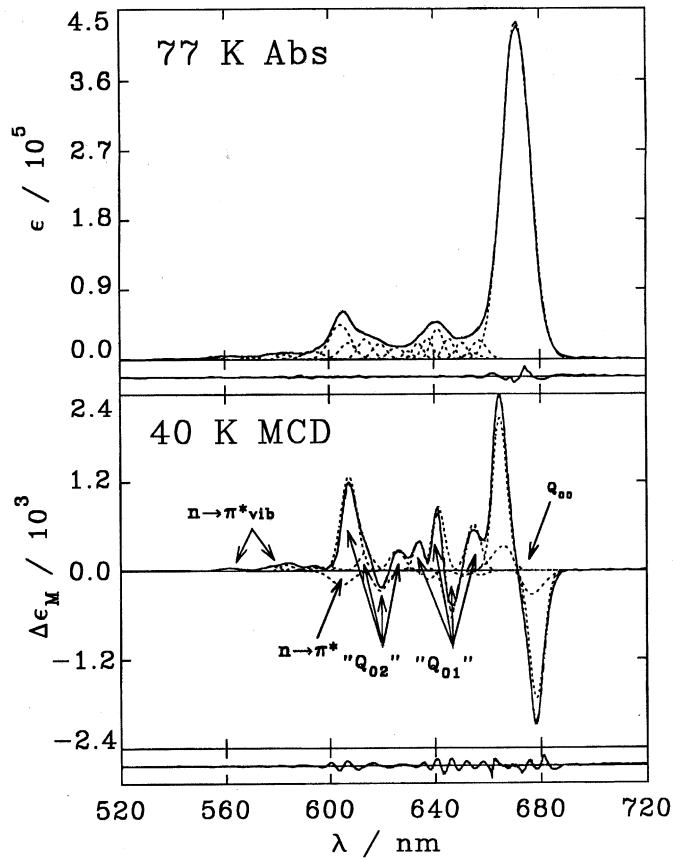

Fig. 8. Spectral deconvolution analysis of the Q band region of the absorption and MCD spectra of (CN^-)ZnPc [20]. Identical bandwidths and centers are used to fit the MCD and absorption spectra recorded at 40 and 77 K on a 5:2 dimethyl formamide-dimethyl acetamide vitrified solution. Solid, dashed and dotted lines represent the experimental and calculated spectral data and the component deconvoluted B terms, respectively. All the MCD bands used in this analysis are B terms to the blue of the main Q_{oo} band. The $n \rightarrow \pi^*$ bands near 605 nm and its associated vibronic progression are indicated. The residual of the fit plotted at the bottom of the plot shows the difference between the experimental and calculated MCD data. Reproduced with permission from Ref. [20].

region [20] recorded at cryogenic temperatures indicates that the bands to the blue of the main Q_{00} band at 670 nm are all Gaussian-shaped B terms. A much greater resolution is obtained from data recorded within vitreous optically transparent solvent mixtures due to the 'freezing out' of the multiplicity of solvation environments present in solution at room temperature. The energies of the vibrational bands identified by spectral deconvolution were in good agreement with those reported in the Shpol'skii matrix emission studies of Huang et al. [55,56]. These authors proposed that there is a z-polarized transition at 604 nm which gives rise

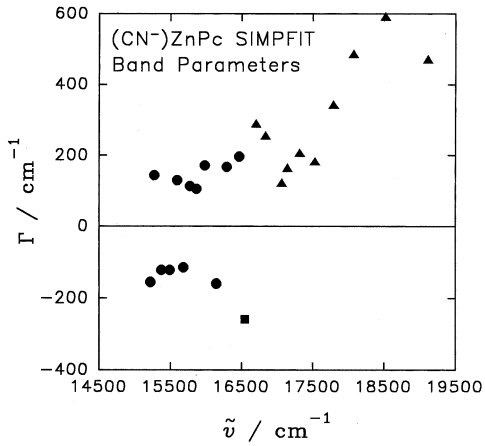

Fig. 9. Trends in the bandwidths of bands used in the fit of the absorption (at 77 K) and MCD (at 40 K) spectra of (CN^-)ZnPc shown in Fig. 8 [20]. The bandwidths are plotted with a sign depending on whether they are associated with positive or negative B terms in the MCD spectrum as a function of band energy. There are two distinct groups of bands to the red and blue of the 605 nm band. The circles represent the 'Q_{01}' and 'Q_{02}' bands associated with the repeating pattern of positive and negative B terms. The bandwidths of vibronic overtones should remain constant (here at about 200 cm^{-1}). The triangles represent the broader set of weaker positive B terms to the blue of the 605 nm band which are believed to be associated with a second electronic transition associated with an $n\pi^*$ excited state. Reproduced with permission from Ref. [20].

to a second set of weak vibrational bands to the blue of the Q transition since the fluorescence excitation and emission spectra deviated significantly from the anticipated mirror image pattern. Our deconvolution analysis [20] (Fig. 8) identified four intense B terms in a $+/-/+/+$ pattern in the order of ascending energy labeled 'Q_{01}' which is followed by a second set of $+/-/+/+$ bands 700 cm^{-1} to the blue labeled 'Q_{02}'. Huang et al. [55,56] proposed that this second repeating set of Q_{vib} bands are overtones of the first sequence which arise from a second quantum of vibrational energy from a totally symmetric a_{1g} vibrational mode. At the high energy edge of the 'Q_{02}' sequence there is a marked difference in the energies of the main absorption and MCD intensity at ca. 600 nm at the energy of Huang et al.'s proposed $n \rightarrow \pi^*$ band. The bands to the blue of the negative B term at 604 nm are all positive B terms and are significantly broader than the Q_{vib} bands to the red. Under D_{4h} symmetry this is the pattern that would be expected for bands arising from the z-polarized $n \rightarrow \pi^*$ transition out of the aza-nitrogen lone-pair orbitals proposed by Huang et al. [55,56]. Although our ZINDO calculations predict that the $n \rightarrow \pi^*$ band should sit within the UV region (Table 2), Schaffer et al.'s extended Hückel calculations [4] predict that this band is close in energy to the Q_{oo} band.

4. Spectral band assignments of radical species using spectral band deconvolution

4.1. The $[MPc(-1)]^+$ species

The band assignment of main group metal $[MPc(-1)]^+$ species is more complicated than that of $MPc(-2)$ complexes since there is a marked solvent and temperature dependence in the spectral data. $[MPc(-1)]^+$ cannot be generated with isosbestic spectral changes due to extensive dimerization [8,10,11,17,19]. The ground-states of divalent, main group D_{4h} $[MPc(-1)]^+$ species are $^2A_{1u}$, while the accessible $\pi \rightarrow \pi^*$ excited states are ^2E_g (x/y-polarized). Fig. 10 shows the absorption and MCD data for the monomeric and dimeric species of $[MgPc(-1)]^+$. The monomeric species is characterized by a Q band near 825 nm, then a strong B term under the 505 nm band, and a series of bands below 450 nm. A similar pattern is seen for the dimeric $([MgPc(-1)]^+)_2$ at 200 K (Fig. 11), with the major bands shifting slightly to the blue. Analysis of the Q band region is straightforward in both species. Spectral deconvolution of the spectral data of the monomeric species identified two additional A terms to the red of the B1/B2 region at 387 and 413 nm

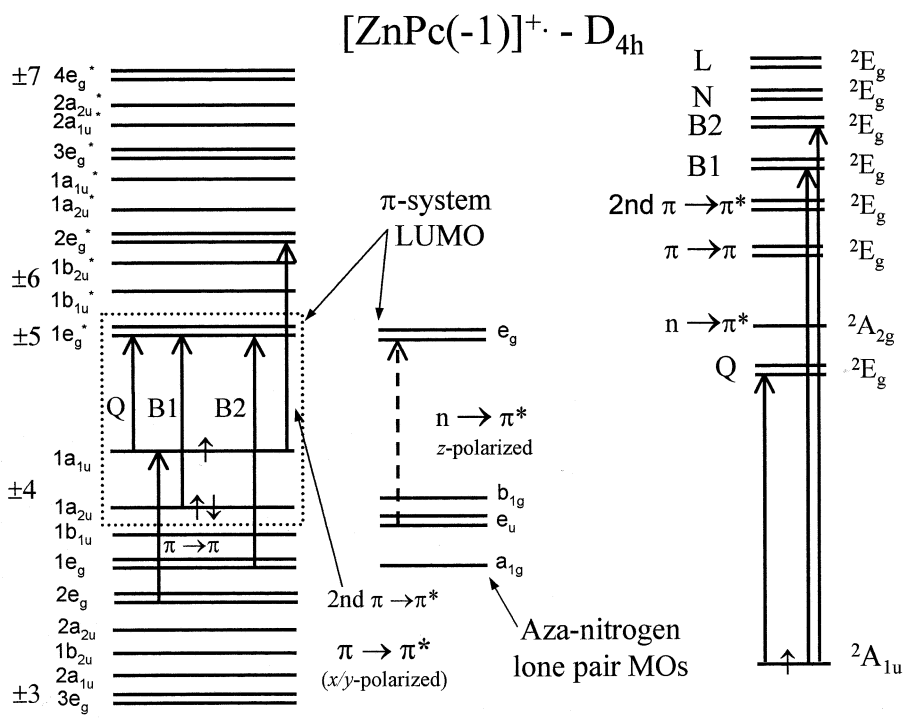

Fig. 10. Molecular orbital and excited state energy level diagram for the π-system and aza-nitrogen lone pair orbitals of $[ZnPc(-1)]^+$ assuming D_{4h} symmetry [35]. The orbital ordering on the left is based on the results of our ZINDO calculation (Table 1). See caption for Fig. 3 for other details.

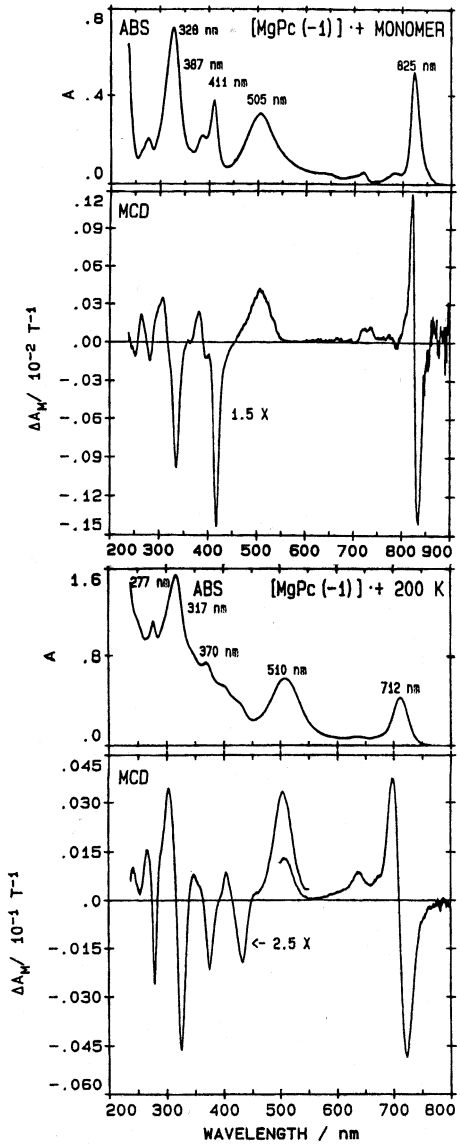

Fig. 11. The absorption and MCD spectra of $[MgPc(-1)]^+$ prepared photochemically at room temperature and recorded at 298 K (monomer) and at 200 K (dimer) in CH_2Cl_2. Reproduced with permission from Ref. [19].

and an intense B term at 509 nm [8–11,17,19] (Fig. 12). The 509 nm B term and broad absorption band was recently re-assigned [35] to an $n \rightarrow \pi^*$ transition linking the lone pair orbitals of the aza-nitrogens and the LUMO of the π-system. Since the 509 nm band is an intense z-polarized Faraday B term rather than an x/y-polarized A term like the other major bands in the MCD spectrum, the excited state is clearly

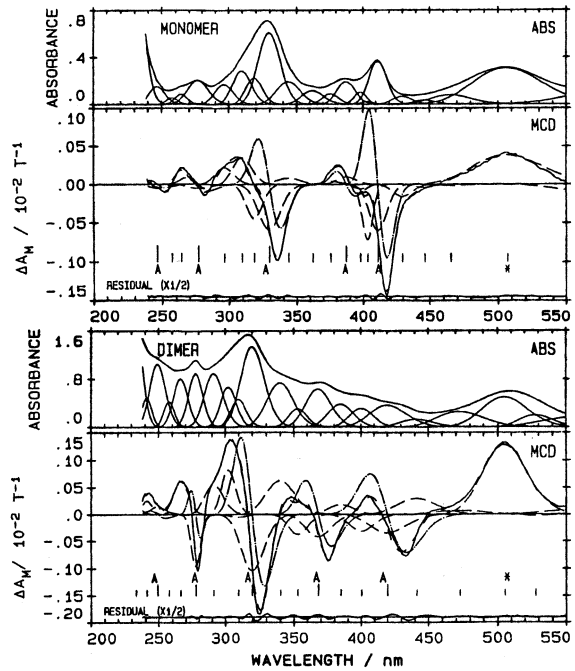

Fig. 12. Spectral deconvolution analysis of the absorption and MCD spectra of the monomeric $[(im)_2MgPc(-1)]^+$ and dimeric $[(im)_2MgPc(-1)]_2^{2+}$ species in the 200–550 nm region. The five transitions to degenerate excited states are marked with an 'A', and the associated A terms are shown as dotted lines. The intense broad band at 510 nm marked with an '*' is completely accounted for by a single B term, indicating that there is no degeneracy in the associated excited state. Reproduced with permission from Ref. [19].

non-degenerate. Deconvolution of the data for the dimeric species (Fig. 12) shows that a single MCD B term accounts completely for the observed spectral envelope near 510 nm. The additional A term at 413 nm of the monomeric species has been assigned to the lowest energy $\pi \rightarrow \pi$ transition into the partially filled HOMO (Figs. 10 and 11) [19,35]. The ZINDO calculation predicts that the A term identified at 387 nm by spectral deconvolution [19] of the spectra of monomeric $[MgPc(-1)]^-$ arises primarily from the second $\pi \rightarrow \pi^*$ transition as it mixes much more significantly with the other higher energy $\pi \rightarrow \pi^*$ transitions than is the case in the $ZnPc(-2)$ spectrum. The major contribution to the A terms at 330, 315 and 275 nm is predicted to be the B1, B2 and $1a_{1u} \rightarrow 3e_g^*$ transition that gives rise to the N band of $MPc(-2)$, respectively (Tables 1 and 2).

4.2. The [MPc(−3)]$^-$ species

The $[MPc(-3)]^-$ species of main group metals can be generated photochemically in aprotic solvents using electron donors such as hydrazine [16]. Fig. 12 shows the

absorption and MCD spectra for $[ZnPc(-3)]^-$ at room temperature and at cryogenic temperatures. There are no major changes in MCD signal intensity over a range of 250 K within the MCD spectrum. This indicates, unambiguously and definitively, that the cryogenic temperature MCD spectrum of the one-electron ring reduced species is completely dominated by B terms, rather than the temperature dependent C terms, despite the fact that a ground state of ^2E_g would be anticipated [21]. There is clearly a substantial static Jahn–Teller splitting of the ground state. We have analyzed the MCD data (Figs. 4 and 13) to suggest that the separation of the coupled B terms was due to a loss in planarity in the non-aromatic anion radical ring. In the absence of X-ray crystallographic data C_{2v}(III) symmetry has been assumed for $[ZnPc(-3)]^-$ in Fig. 14, since the MOs obtained in our ZINDO calculation for the absorption spectrum of $[ZnPc(-3)]^-$ appear to have C_{2v}(III) symmetry properties [57] if ring saddling occurs [35]. Under C_{2v}(III) symmetry the

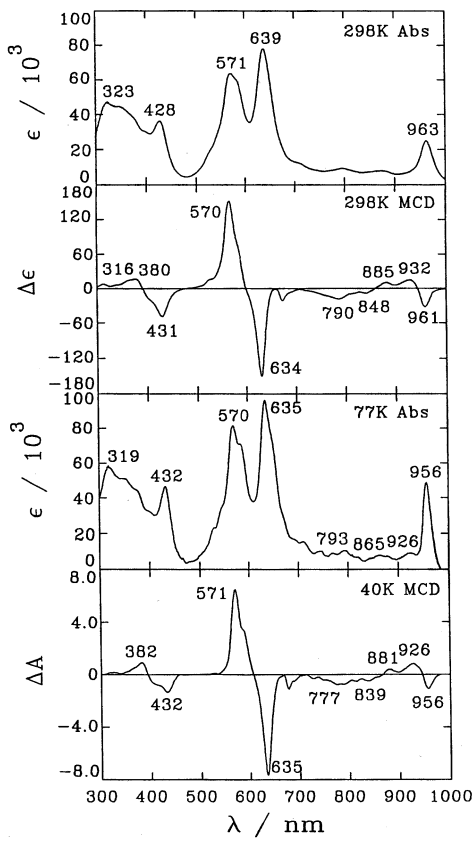

Fig. 13. The absorption and MCD spectra of $[ZnPc(-3)]^-$ prepared photochemically at room temperature and recorded at 298 and 77 K. Identical bandwidths and centers are used to fit the MCD and absorption spectra recorded at 40 and 77 K on a 5:2 dimethyl formamide–hydrazine hydrate vitrified solution. Reproduced with permission from Ref. [12].

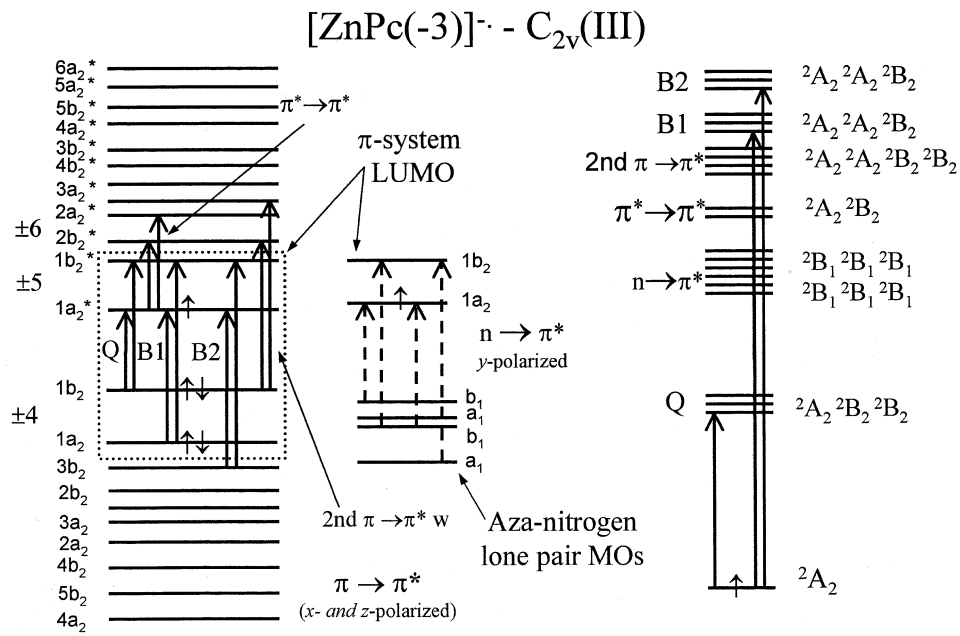

Fig. 14. Molecular orbital and excited state energy level diagram of $[ZnPc(-3)]^{-}$ assuming C_{2v}(III) symmetry. The C_2 axis sits within the plane of the ring due to ring ruffling/doming when aromaticity is lost through the addition of an extra electron to the π-system [35]. Transitions that give rise to *x*- or *z*-polarized bands are represented with solid lines. Dashed lines are used for *y*-polarized transitions. The $n \rightarrow \pi^*$ transitions are placed between the Q_{vib} and B1 transitions on the basis of the assignment of the Q region of (CN)ZnPc(−2) [20].

C_2 axis does not correspond with the C_4 symmetry axis of MPc(−2) but sits within the plane of the ring.

A plot of the band centers and bandwidths obtained through the spectral deconvolution of the MCD and absorption data of $[ZnPc(-3)]^{-}$ [16] recorded at cryogenic temperature data identified three distinct sets of coupled, oppositely signed B terms observed in the MCD spectrum of $[ZnPc(-3)]^{-}$, at 958/925, 635/569 and 434/383 nm (Figs. 15 and 16) [16]. Hochstrasser and Marzzacco demonstrated empirically that bands associated with ππ* excited states in heteraromatic ring systems are broadened significantly when there is an $n\pi^*$ state sitting at lower energy [58]. The pair of bands centered on 958 and 925 nm exhibit a marked inequivalence in B term intensity. This would tend to indicate that they arise from one-electron transitions where the electron goes into the partially filled Jahn–Teller split LUMO. Since these are the lowest energy bands within the $[MPc(-3)]^{-}$ spectral envelope they can be assigned to the Q transition (Fig. 15). The weak bands immediately to the blue are believed to be vibronic in origin. The equivalence in the B term intensities of the intense 635 and 569 nm bands is consistent with field-induced mixing between two major one-electron transitions into a pair of close lying empty orbitals. These bands have therefore been assigned to the $\pi^* \rightarrow \pi^*$

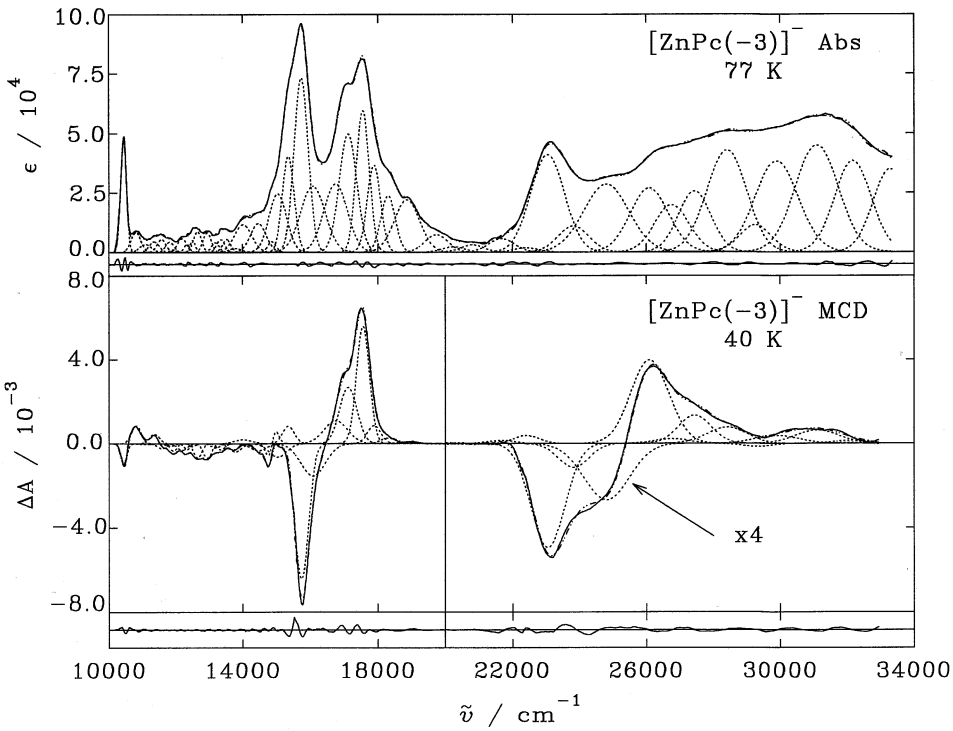

Fig. 15. Complete set of 45 Gaussian bands required to fill the absorption and MCD band envelopes of $[ZnPc(-3)]^-$. One additional band was required to account for the Q_{00} band associated with a slight impurity of $ZnPc(-2)$. Reproduced with permission from Ref. [16].

transition (Fig. 15). Our ZINDO calculation (Table 3) provided strong evidence for this assignment as intense calculated bands at 600 and 588 nm were predicted to arise primarily with the $\pi^* \rightarrow \pi^*$ transition. The complexity seen in the absorption spectrum in this region and significant band broadening to the blue is probably connected to the presence of weak $n \rightarrow \pi^*$ bands such as those seen in the spectra of $ZnPc(-2)$ and $[ZnPc(-1)]^+$ [18]. The spectral deconvolution analysis of the 350–450 nm region indicated that there are two major overlapping sets of B terms exhibiting the same $-/+/+$ B term sign pattern exhibited in the near IR (Fig. 15). Michl has demonstrated that the signs of pairs of oppositely signed B terms of cyclic polyene molecules in which the degeneracy has been broken by a perturbation to the molecular geometry [27,28] is determined by the relative magnitude of the OAM associated with the ground and excited states rather than by the band polarizations. The ZINDO calculation predicts that the second $\pi \rightarrow \pi^*$ transition, B1 and B2 transition contribute significantly to the numerous bands in this region (Table 3). The predicted degree of mixing between the excited states is so great that the assignment of individual bands to specific one-electron transitions would not be particularly meaningful in this region of the spectrum (Table 3).

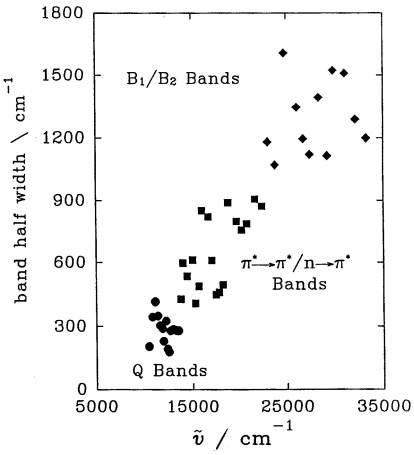

Fig. 16. Scatter plot of the bandwidths as a function of the band centers derived from the deconvolution analysis shown in Fig. 18. The symbols represent groups of clusters of bands with similar widths believed to be associated with the following transitions: Q (circles), $\pi \rightarrow \pi^*$ and possibly $n \rightarrow \pi^*$ (squares) and B1/B2 (diamonds). Reproduced with permission from Ref. [16].

Under C_{2v}(III) symmetry, the Q, B1 and B2 transitions of ZnPc(-2) and the new $\pi^* \rightarrow \pi^*$ transition, are allowed for [ZnPc(-3)]$^-$ with x- and z-polarized bands significantly separated in energy (Fig. 15). The z-axis of [ZnPc(-3)]$^-$ under C_{2v}(III) symmetry corresponds to the y-axis of ZnPc(-2) under D_{4h} symmetry. A further effect of C_{2v}(III) symmetry is to allow $\pi \rightarrow \pi^*$, $\pi^* \rightarrow \pi^*$, and $n \rightarrow \pi^*$ transitions which would be parity forbidden under D_{4h} symmetry (Table 3). The poorer orbital overlap of the ground and excited states of these transitions significantly reduces the intensity of the associated spectral bands relative to the bands that arise from the $\pi^* \rightarrow \pi^*$ and $\pi \rightarrow \pi^*$ transitions that would be parity allowed under D_{4h} symmetry. The Q, second $\pi \rightarrow \pi^*$, and B1 transitions of the neutral MPc(-2) species, and the new $\pi^* \rightarrow \pi^*$ transitions are, therefore, expected to be responsible for the major bands in the spectral envelope between 250 and 1000 nm.

5. Assignment of the spectra of the [MPc(-4)]$^{2-}$ species based on ZINDO calculations

A number of research groups have used spectroelectrochemical cells to record spectra of the [MPc(-3)]$^-$ and [MPc(-4)]$^{2-}$ species of a variety of MPc complexes [59–66]. Clack and Yandle reported the band maxima and relative intensities of a wide range of [MPc($-(2+n)$)]$^{n-}$ ($n = 1 \rightarrow 4$) species generated chemically in vacuo over sodium films [59]. Linder et al. used this technique to record room temperature absorption and MCD spectral data for the four reduced species of MgPc [67]. In the absence of the Jahn–Teller splitting there would be a $^3A_{2g}$ ground-state and ^3E_u excited states for the major $\pi \rightarrow \pi^*$ and $\pi^* \rightarrow \pi^*$ transi-

tions. This can be ruled out since no derivative-shaped A terms were observed in the MCD spectrum with band centers corresponding to those of the major absorption bands (Fig. 4). Since there is no EPR signal [68,69] for the $[MPc(-4)]^{2-}$ species, we can conclude that the two additional electrons are paired in the lower energy orbital of a Jahn–Teller split LUMO (Fig. 4). This results in a complete lifting of the ground and excited state orbital degeneracies similar to that seen in the $[MPc(-3)]^{-}$ species. Significant differences can be expected in the Q and B1 transitions of $[MPc(-3)]^{-}$ and $[MPc(-4)]^{2-}$ since electrons from lower orbitals cannot enter the filled $1b_{2g}^{*}$ orbital (Fig. 17) (D_{2h}(II) symmetry [57] has been assumed for the $[ZnPc(-4)]^{2-}$ [35]). The MCD band arising from $\pi \rightarrow \pi^{*}$ transitions will be very weak unless there is mixing with a state that arises from another transition. The absorption band at 805 nm can therefore be assigned to the Q transition, since there is no corresponding MCD signal in this region of the spectrum (Fig. 4). The pair of coupled B terms at 506 and 620 nm can be assigned to the $\pi^{*} \rightarrow \pi^{*}$ transition into the empty $1a_{u}^{*}$ and $1b_{1u}^{*}$ orbitals. The field-induced mixing between these states gives rise to the intense pair of coupled oppositely

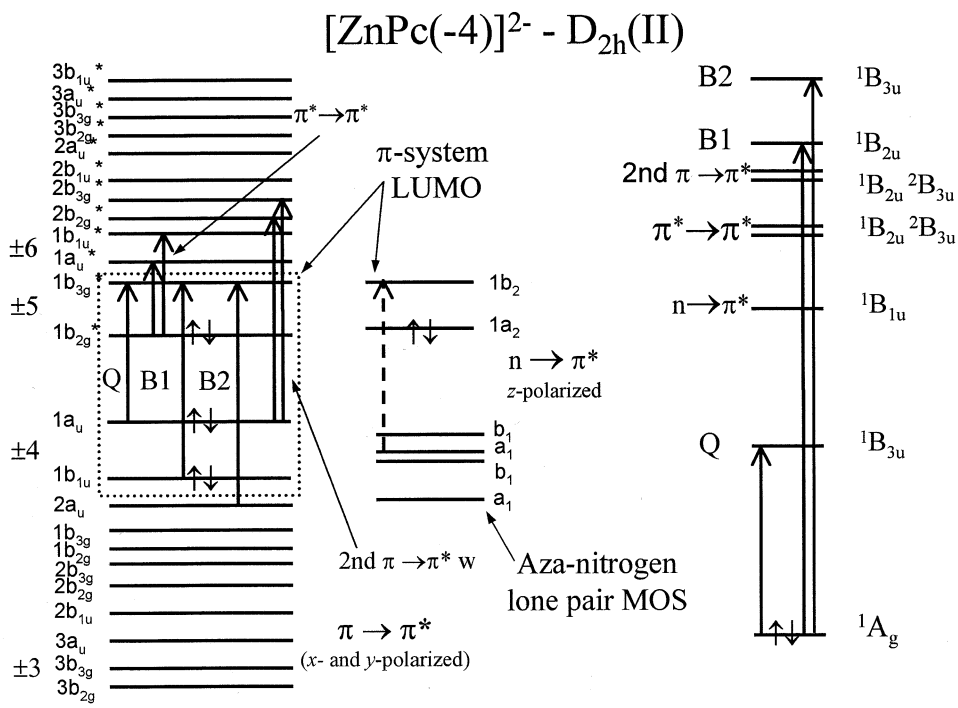

Fig. 17. Molecular orbital and excited state energy level diagram level diagram of $[ZnPc(-4)]^{2-}$ assuming D_{2h}(II) symmetry. The major C_2 axis is perpendicular to the plane of the ligand π-system. Transitions that give rise to *x*- or *y*-polarized bands are represented with solid lines. Dashed lines are used for *z*-polarized transitions. The $n \rightarrow \pi^{*}$ transitions are placed between the Q_{vib} and B1 transitions on the basis of the assignment of the Q region of (CN)ZnPc(−2) [20].

signed B terms, which dominates the MCD spectrum in this region of the spectra of both $[MPc(-3)]^-$ and $[MPc(-4)]^{2-}$. In the 300–450 nm region, the second $\pi \rightarrow \pi^*$ and B1 excited states can couple with each other and to other higher energy states and as a result significant MCD intensity is seen [35]. ZINDO calculations predicted that the second $\pi \rightarrow \pi^*$ transition is the only $\pi \rightarrow \pi^*$ transition to give rise to significant intensity in this portion of the spectrum (Table 4).

6. Assignment of the spectra of the $[MPc(-5)]^{3-}$ and $[MPc(-6)]^{4-}$ species

EPR data for $[MPc(-5)]^{3-}$ are consistent with a ground-state containing a single unpaired electron [68,69]. An initial band at 1125 nm in the spectrum of $[MgPc(-5)]^{3-}$ is assigned to the Q transition [59,67]. Although the resolution of Linder's absorption spectrum is low, the band appears to be a simple Gaussian curve and there are apparently no associated vibrational bands [67]. The occupation of both the $1a_2^*$ and $1b_2^*$ orbitals of the Jahn–Teller split LUMO can be expected to lead to two separate $\pi^* \rightarrow \pi^*$ transitions. The broad absorption bands at 589 and 825 nm [59,67] are assigned to these transitions. The assumption is made that individual x- and z-polarized bands are not fully resolved in the absorption spectrum due to the band broadening effects that were seen in the $\pi^* \rightarrow \pi^*$ region of the $[ZnPc(-4)]^{2-}$ spectrum. A weak band at 338 nm is assigned to the second $\pi \rightarrow \pi^*$ transition (Fig. 4) [59,67]. As would be expected, EPR measurements for $[ZnPc(-6)]^{4-}$ have indicated that the ground-states of main group $[MPc(-6)]^{4-}$ species are diamagnetic [68,69] as the LUMO of the neutral species is fully populated. D_{4h} symmetry has been assumed for this species [35]. The $1e_g^*$ orbital are almost degenerate within our ZINDO calculations. The major transitions give rise to ^1E_u $\pi\pi^*$ excited states similar to those associated with the $ZnPc(-2)$ and $[ZnPc(-1)]^+$ species. The absorption spectrum of $[MgPc(-6)]^{4-}$ reported by Linder et al. [67] is dominated by two intense absorption bands at 625 and 840 nm. As the $1e_g^*$ orbital is fully occupied, the near IR–vis region of the spectrum can be expected to be dominated by the two $\pi^* \rightarrow \pi^*$ transitions from the $1e_g^*$ orbital to the symmetry split $1b_{1u}^*$ and $1b_{2u}^*$ orbitals. Linder et al. [67] report an MCD signal for the 840 nm band which could be interpreted as a broad A term. The absorption spectrum of $[MgPc(-6)]^{4-}$ contains an additional intense band in the UV region (Table 4) which can be assigned to the second $\pi \rightarrow \pi^*$ transition although our ZINDO calculation suggests that most of the absorption intensity in this region actually arises from a series of close lying higher energy $\pi^* \rightarrow \pi^*$ transitions [35].

7. Summary of the assignments for the $[MPc(-(n+2))]^{n-}$ $(n = -1 \rightarrow 4)$ species

By measuring absorption and MCD spectral data for the main group $MPc(-2)$ [8–12,17–20,35], $[MPc(-3)]^-$ [16,21], $[MPc(-4)]^{2-}$ [35] species and using the data of Linder [67] for $[MPc(-5)]^{3-}$ and $[MPc(-6)]^{4-}$ together with the absorption data of Clack and Yandle [59], we have been able to propose a unified

assignment of the optical spectra of the $[MPc(-(n+2))]^{n-}$ $(n=-1\rightarrow 4)$ species. Since the same set of $\pi\rightarrow\pi^*$, $\pi\rightarrow\pi$, and $\pi^*\rightarrow\pi^*$ transitions give rise to bands in the neutral, ring-oxidized cation and ring-reduced anion species of main group metal phthalocyanines, it is possible to compare the relative energies of the major transitions of each species by plotting the energies of the band centers against the number of electrons added or removed from the MPc ring (Fig. 18). The high level of agreement between the observed and calculated band energies across the various oxidation states so the one electron transitions identified in Fig. 18 only represent

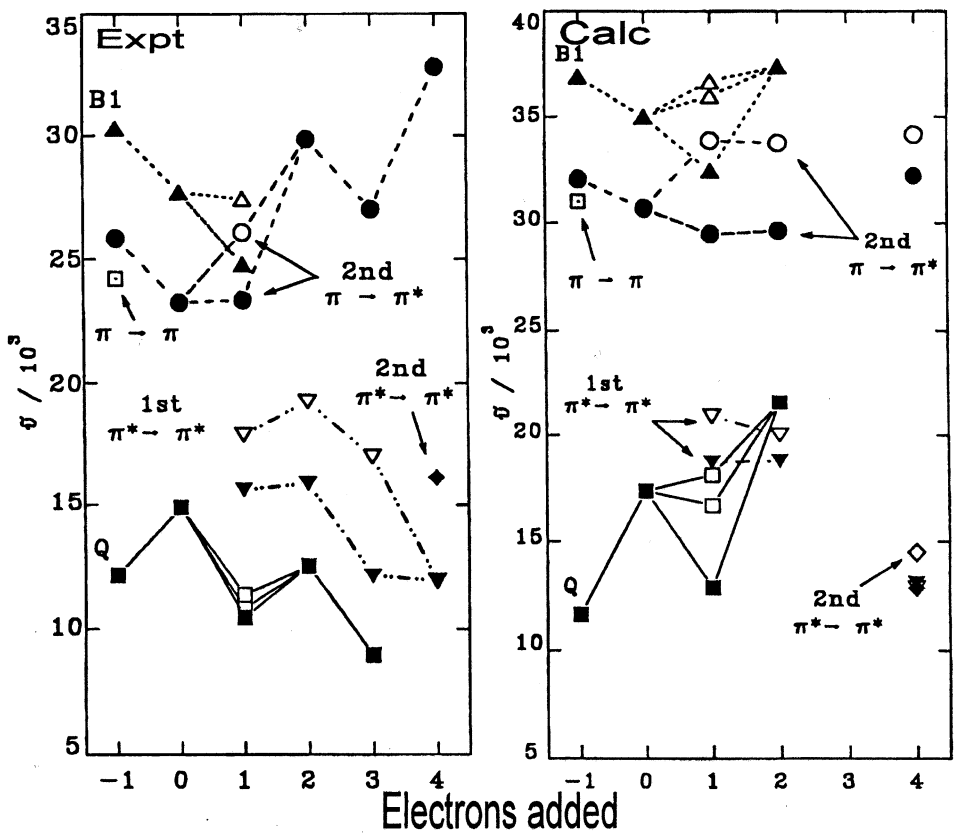

Fig. 18. Relative energies of the major electronic transitions both observed and calculated for the π-system transitions of closed shell MPc neutral, ring-oxidised, and ring-reduced species. Observed experimentally [18–21,59] in the case of MgPc and ZnPc by optical spectroscopy (left) and calculated for ZnPc by the ZINDO program with details shown in Tables 1–4 (right). The x-axis indicates the number of electrons removed or added to the ring, where 0, denotes the neutral $MPc(-2)$ complex. Different line types and symbols are used to link the bands of each major transition. Since for each ring oxidation state, different sets of transition are possible not all lines continue across all oxidation states. The labels indicate the band assignments discussed in the text. Solid and hollow symbols are used to indicate excited states associated with oppositely signed coupled B terms in species subject to a static Jahn–Teller distortion. Reproduced with permission from Ref. [35].

a first order assignment. Although the one-electron energy differences between the orbitals would normally be expected to be one of the most important factors determining the energies of the transitions, this had not previously been demonstrated over such a wide range of metal phthalocyanine redox states [35]. On the basis of this analysis, we have been able to construct a complete band assignment by Clack and Yandle [59] for AlClPc(−2), NiPc(2), MnPc(−2), CoPc(−2) and Fe(II)Pc(−2) in which charge transfer bands are also sometimes present [70].

8. Assignment of transition metal phthalocyanine spectral data

The assignment of the spectra of main group phthalocyanines provides the characteristic marker bands for the ring oxidized $[MPc(-1)]^{+}$, neutral MPc(−2), and ring-reduced $[MPc(-3)]^{-}$, $[MPc(-4)]^{2-}$, $[MPc(-5)]^{3-}$, and $[MPc(-6)]^{4-}$ species of the much more complex spectra of transition metal phthalocyanine cation radical, neutral, and anion radical species, where reduction and oxidation at the metal center is also possible. A major complication in the assignment of the optical spectra of the transition metal species is the potential presence of metal to ligand (MLCT) and ligand to metal (LMCT) charge transfer bands throughout the UV–vis–near IR region. Even when metal oxidation or reduction does not occur, the optical data of the ring oxidized or ring reduced species does not necessarily closely resemble those of the main group species. The spectral data recorded following oxidation of Ru(II)Pc(−2) shows that this is solely ring oxidation and the product is $[Ru(II)Pc(-1)]^{+}$ [71]. The radical cation that is formed photochemically exhibits a spectrum that closely resembles that of $[MgPc(-1)]^{+}$ in the 450–900 nm region, which indicates that charge transfer bands are either very weak or nonexistent within this spectral region. On the other hand, the spectral data for FePc complexes are much more complex, the MCD data for the Fe(II)Pc(−2) [13] species are temperature dependent indicating ground state degeneracy. In the case of low spin Fe(II)Pc(−2), this is a result of mixing with the MLCT states.

We have chosen to use the analysis of the absorption and MCD spectral data for low spin Fe(III)Pc(−2) [13] as our example because these systems are extremely complicated and require some detail in order to show how the coupling of the deconvolution analysis with the group theoretical predictions leads to assignments essentially unobtainable by other techniques. Fig. 19 shows the absorption and MCD data for $Na[(CN)_2Fe(III)Pc(-2)]$ recorded from vitreous samples (top; absorption spectrum measured at 77 K, MCD spectrum measured at 4 K) and solutions (bottom; room temperature for both absorption and MCD spectra) [13]. The combination of the paramagnetic, low spin Fe(III) and the presence of charge transfer transitions (LMCT and MLCT), results in a ground state that is orbitally degenerate, $^{2}E_{g}$, and an MCD spectrum that is highly temperature dependent. The MCD signature at 4 K is inverted in sign when compared with the room temperature data, due to the dominance of the C terms at 4 K [13]. The origin of this extensive C term signal is the splitting of the spin-orbit ground state and the subsequent depopulation of the upper states results in significant increases in

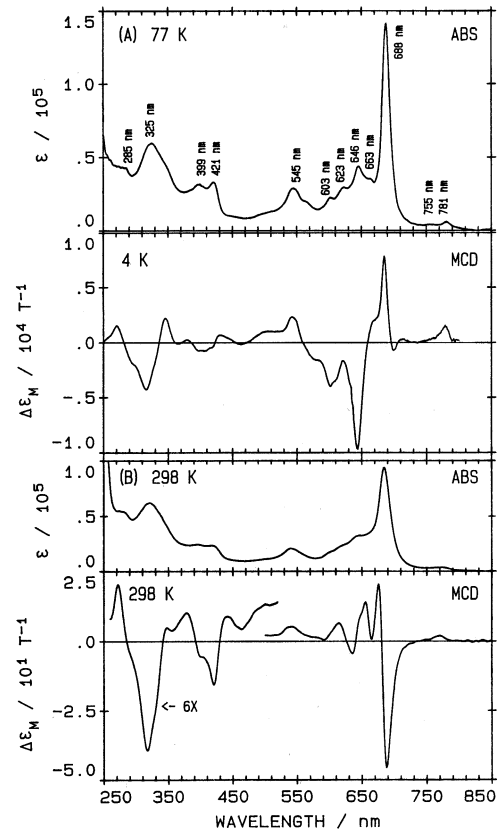

Fig. 19. Absorption and MCD spectral data recorded at 298 K (bottom) and 77 K (absorption) and 4 K (MCD) (top) for low-spin $Na[(CN^-)_2Fe(III)Pc(-2)]$ in CH_2Cl_2. The data show how the ground state of the $[(CN^-)_2Fe(III)Pc(-2)]^+$ is dominated by C terms so that the MCD signal inverts between room temperature and 77 K. Deconvolution analysis is shown in Fig. 22. Reproduced with permission from Ref. [13].

Gaussian-shaped C terms in place of derivative-shaped A terms, see figure 8 in Ref. [13]). Fig. 20 shows the spectral band deconvolution analysis of the low temperature data. Forty four bands were required to fill the absorption and MCD envelopes between 250 and 800 nm. Detailed analysis of the MCD data was required before the absorption data could be adequately interpreted. As with the spectral data of the main group species, spectral fitting is necessary in order to determine the band parameters and polarization properties. These parameters allow the construction of an energy level diagram that shows the energies of all transitions in the spectrum. Assignments for the bands can be made based on association with the main group analysis and the band properties from the MCD spectral data (Fig. 21). It is the alignment of the sign of the C term in the MCD spectrum recorded at ca. 4 K that provides the key to the assignment. The sign can be readily

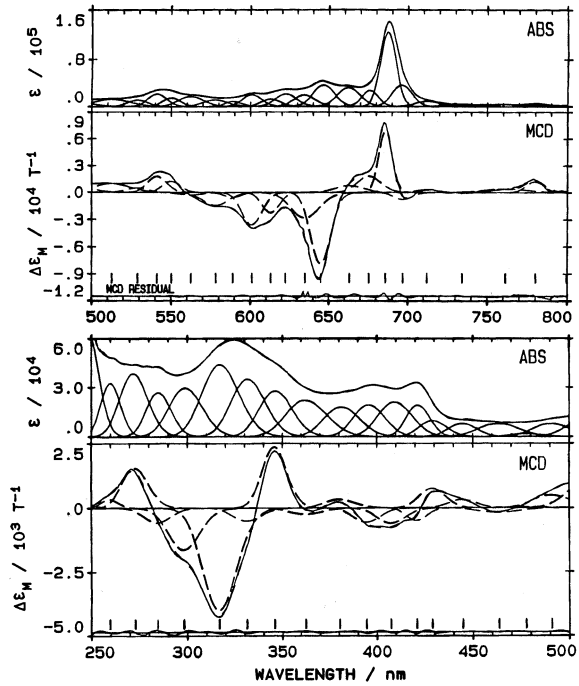

Fig. 20. Spectral deconvolution analysis of the absorption and MCD spectral data recorded at 77 K (absorption) and 4 K (MCD) for low-spin $Na[(CN^-)_2Fe(III)Pc(-2)]$ in CH_2Cl_2. The Q band region (top) is dominated by the C term at 680 nm and the close-lying LMCT band near 640 nm. The B band region, (bottom) is highly complex due to the presence of charge transfer bands. Reproduced with permission from Ref. [13].

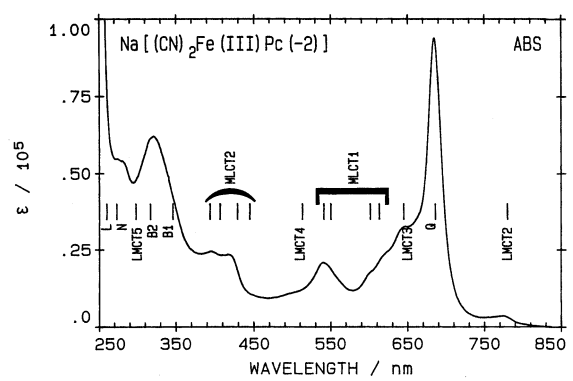

Fig. 21. Assignment of the absorption spectrum of low spin $Na[(CN^-)_2Fe(III)Pc(-2)]$ in CH_2Cl_2. Several regions of LMCT and MLCT bands overlay the ring-based transitions. Reproduced with permission from Ref. [13].

calculated for all possible one-electron transitions between the ring and the d-orbitals of the Fe(III), using these data this and with the deconvoluted data providing the sign and energies of individual bands, we can align predicted transitions with observed MCD bands, see table 3 in Ref. [13]) (Fig. 21). The complexity of the optical spectra of the paramagnetic metal–phthalocyanines becomes clear from the overlap of CT bands throughout the 250–800 nm spectral range, so that even the Q_{vib} region at 650 nm comprises an overlap of CT and vibrational bands. This coincidence in energy levels suggests that resonance Raman might provide useful information on the co-ordination state of the metal.

Fig. 22 shows a very detailed diagram constructed from spectral deconvolution of the absorption and MCD data of the low spin (CN^- L. S.) Na[$(CN)_2$Fe(III)Pc(−2)] (shown in Fig. 20), together with data from analyses of the intermediate spin (Fo^- I. S.) Na[(formate)$_2$Fe(III)Pc(−2)] [72], [MgPc(−1)]$^+$ [19] and Fe(III)Pc(−1) [72]. Clearly, the electronic structure of the FePc complexes is dominated by the presence of charge transfer bands. Oxidation of the phthalocyanine ring in Fe(III)Pc results in a very complex optical spectrum as it is clear that the coupling of the radical ground state of the ring to the charge transfer states of the Fe(III) results in a continuum of major electronic bands that span the 250–900 nm region (unpublished data). The MCD data allow identification of regions of bands that relate to the bands observed in the main group MPc species described above. At 300 nm, the MCD signatures of the B1 and B2 bands are clearly observed while between 450 and 550 nm we can identify transitions that may be associated with the $n \rightarrow \pi^*$ observed near 500 nm in main group species. The Q band signature at 800 nm along with a series of MCD bands that suggest a set of vibronic bands on the high-energy side. However the situation is so complicated that definitive assignment will require analysis of the spectral data recorded at low temperatures of a series of axially-substituted species. The energies of the bands observed in the absorption and MCD data and identified by the deconvolution calculation were used in the construction of Fig. 22, in which the spectral data for the main group radical cation species, [MgPc(−1)]$^+$, are compared with the data for this low spin Fe(III) species [11].

9. Conclusions

Spectral band deconvolution analyses based on MCD spectroscopy have provided the essential additional information required to develop a detailed assignment of the complex overlapping absorption spectra of metal phthalocyanine species. Spectral band deconvolution studies of MPc(−2) optical spectra data provided evidence of the presence of a second A term in the B region leading to a modification of the earlier Q, B, N, L and C assignment sequence to contain overlapping B1 and B2 bands. A detailed study of the vibrational envelope to the blue of the Q band in spectra recorded on vitrified solutions at cryogenic temperatures led to the identification of a weak $n \rightarrow \pi^*$ band at 605 nm [20]. Spectral deconvolution studies have been used to fully assign the spectra of [MPc(−1)]$^+$

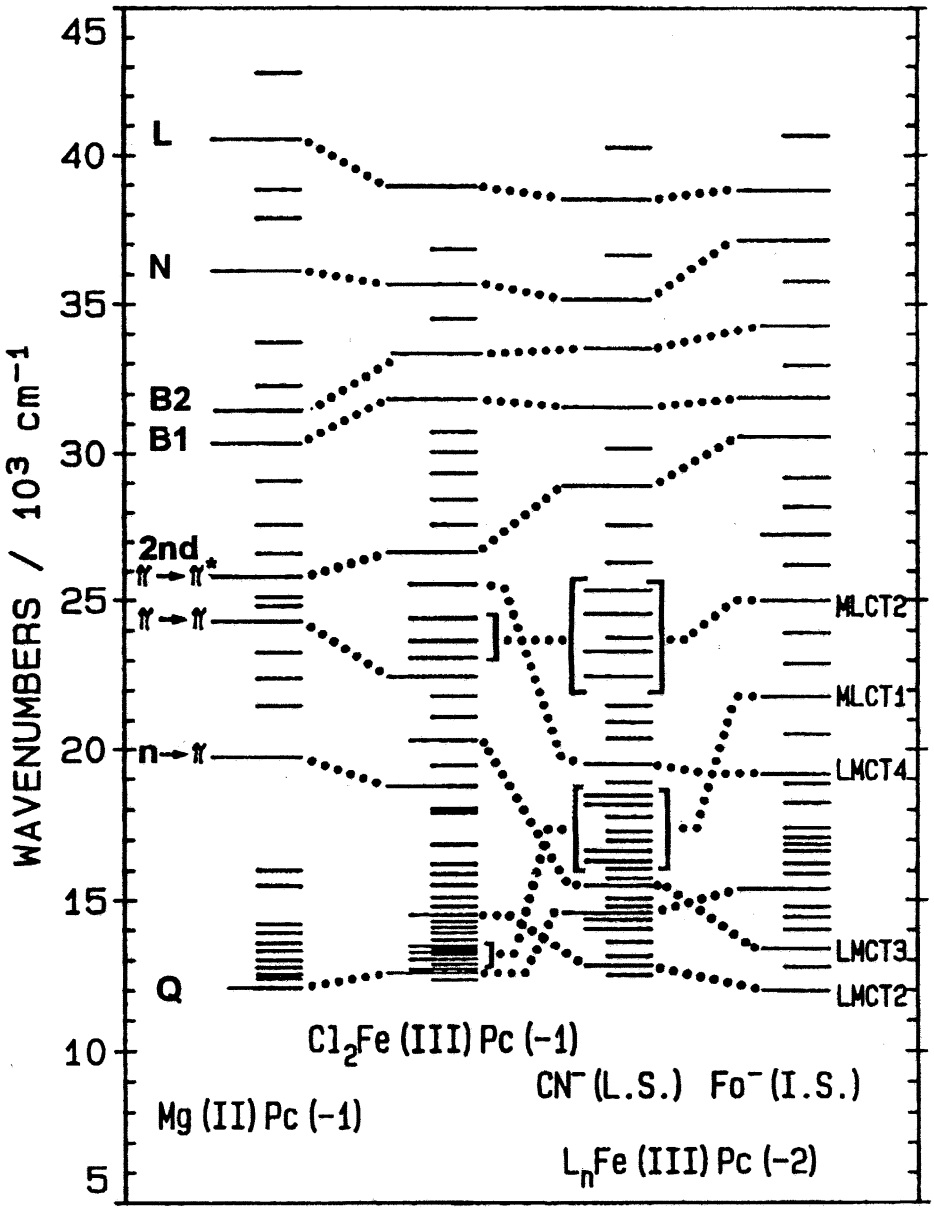

Fig. 22. Energy level diagram assembled from the results of spectral deconvolution of a range of phthalocyanine species. (A) Assignment of the absorption spectrum of monomeric ring-oxidized, $[MgPc(-1)]^{+}$. (B) Data for the ring-oxidized Fe(III)Pc(−1) species. (C) Data for low spin Fe(III)Pc(−2). (D) Data for intermediate spin Fe(III)Pc(−2).

species. A terms associated with monomeric and dimeric species have been identified and assigned on the basis of Gouterman's model. A broad B term at 510 nm has been assigned to an $n \rightarrow \pi^*$ transition [35,54]. The absence of A and C terms in the MCD spectra of $[MPc(-3)]^-$ species represented the first direct spectral evidence that the orbital degeneracies of both the ground and excited states are lifted upon ring reduction. A band assignment for the major x- and z-polarized transitions has been developed which is based upon the band polarization information obtained from the oppositely signed coupled B terms in a band deconvolution analysis of $[ZnPc(-3)]^-$. A general assignment of the major transitions associated with the π-system of the phthalocyanine ring in six different redox states can therefore now be made, based on the results of spectral band deconvolution studies and MO calculations using the ZINDO program on $[MPc(-(n+2))]^{n-}$ $(n = -1 \rightarrow 4)$ species [35].

Acknowledgements

We thank NSERC of Canada for Operating and Equipment grants (to M.J.S.). M.J.S. is a member of the Centre for Chemical Physics at UWO.

References

[1] M. Gouterman, in: D. Dolphin (Ed.), The Porphyrins, Part A, vol. III, New York, Academic Press, 1978, pp. 1–165.
[2] M. Gouterman, J. Mol. Spectrosc. 44 (1972) 37.
[3] M. Gouterman, G.H. Wagniere, L.C. Snyder, J. Mol. Spectrosc. 11 (1963) 108.
[4] A.M. Schaffer, M. Gouterman, C. Weiss, Theor. Chim. Acta 30 (1973) 9.
[5] C. Weiss, H. Kobayashi, M. Gouterman, J. Mol. Spectrosc. 16 (1965) 415.
[6] A.J. McHugh, M. Gouterman, C. Weiss, Theor. Chim. Acta 24 (1972) 346.
[7] The charge on the phthalocyanine ligand (Pc) is shown in brackets throughout.
[8] T. Nyokong, Z. Gasyna, M.J. Stillman, Inorg. Chem. 26 (1987) 1087.
[9] M.J. Stillman, T.N. Nyokong, in: C.C. Leznoff, A.B.P. Lever (Eds.), Phthalocyanine. Principles and Properties, vol. I, New York, VCH, 1989, pp. 133–289 Ch. 3.
[10] M.J. Stillman, in: C.C. Leznoff, A.B.P. Lever (Eds.), Phthalocyanine. Principles and Properties, vol. III, New York, VCH, 1993, pp. 227–296 Ch. 5.
[11] E.A. Ough, M.J. Stillman, Inorg. Chem. 33 (1994) 573.
[12] J. Mack, Ph.D. Thesis, University of Western Ontario, 1994.
[13] E.A. Ough, M.J. Stillman, Inorg. Chem. 34 (1995) 4317.
[14] T.N. Nyokong, Ph.D. Thesis, University of Western Ontario, 1986.
[15] E.A. Ough, Ph.D. Thesis, University of Western Ontario, 1992.
[16] J. Mack, M.J. Stillman, J. Am. Chem. Soc. 116 (1994) 1292.
[17] T. Nyokong, Z. Gasyna, M.J. Stillman, Inorg. Chem. 26 (1987) 548.
[18] E.A. Ough, T. Nyokong, K.A.M. Creber, M.J. Stillman, Inorg. Chem. 27 (1988) 2724.
[19] E.A. Ough, Z. Gasyna, M.J. Stillman, Inorg. Chem. 30 (1991) 2301.
[20] J. Mack, M.J. Stillman, J. Phys. Chem. 95 (1995) 7935.
[21] J. Mack, S. Kirkby, E.A. Ough, M.J. Stillman, Inorg. Chem. 31 (1992) 1717.
[22] Z. Gasyna, W.R. Browett, T. Nyokong, R. Kitchenham, M.J. Stillman, Chemom. Intell. Lab. Syst. 5 (1989) 233.

[23] J. Mack, W.R. Browett, M.J. Stillman (2001) submitted.
[24] CAChe Scientific, PO Box 500, Mail Station 13-400 Beaverton, OR 97077, USA.
[25] S.B. Piepho, P.N. Schatz, in: Group Theory in Spectroscopy with Applications to Magnetic Circular Dichroism, Wiley, New York, 1983.
[26] P.J. Stephens, Adv. Chem. Phys. 35 (1976) 197.
[27] J. Michl, J. Am. Chem. Soc. 100 (1978) 6801.
[28] J. Michl, Pure Appl. Chem. 52 (1980) 1549.
[29] P.R. Bevington, Data Reduction and Error Analysis for the Physical Sciences, McGraw-Hill, New York, 1969.
[30] W. Spendley, G.R. Hext, F.R. Himsworth, Techometrics 4 (1962) 441.
[31] J.A. Nelder, R. Mead, Comput. J. 7 (1965) 308.
[32] M.W. Routh, P.A. Swartz, M.B. Denton, Anal. Chem. 49 (1977) 1422.
[33] P.R. Ryan, R.L. Barr, H.D. Todd, Anal. Chem. 52 (1980) 1460.
[34] J.C. Sutherland, in: D. Dolphin (Ed.), The Porphyrins; Part A, vol. III, New York, Academic Press, 1978, pp. 225–248.
[35] J. Mack, M.J. Stillman, Inorg. Chem. 36 (1997) 413.
[36] G.D. Purvis III, Comp. Aided Mol. Des. 5 (1991) 55.
[37] C.C.J. Roothaan, Rev. Mod. Phys. 23 (1951) 69.
[38] R. McWeeny, G.J. Diercksen, Chem. Phys. 49 (1968) 4852.
[39] M.F. Guest, V.R. Saunders, Mol. Phys. 28 (1968) 819.
[40] J.S. Binkley, J.A. Pople, P.A. Dobosh, Mol. Phys. 28 (1974) 1423.
[41] E.R. Davidson, Chem. Phys. Lett. 21 (1973) 565.
[42] K. Faegri, R. Manne, Mol. Phys. 31 (1976) 1037.
[43] H. Hsu, E.R. Davidson, R.M. Pitzer, J. Chem. Phys. 65 (1976) 609.
[44] J.E. Ridley, M.C. Zerner, Theor. Chim. Acta 32 (1973) 111.
[45] M.C. Zerner, G.H. Loew, R.F. Kirchner, U.T. Mueller-Westerhoff, J. Am. Chem. Soc. 102 (1980) 589.
[46] J.E. Ridley, M.C. Zerner, Theor. Chim. Acta 42 (1976) 223.
[47] A. Bacon, M.C. Zerner, Theor. Chim. Acta 53 (1979) 21.
[48] J. Head, M.C. Zerner, Chem. Phys. Lett. 122 (1985) 264.
[49] J. Head, M.C. Zerner, Chem. Phys. Lett. 131 (1986) 359.
[50] W. Anderson, W.D. Edwards, M.C. Zerner, Inorg. Chem. 25 (1986) 2728.
[51] W.D. Edwards, M.C. Zerner, Theor. Chim. Acta 72 (1987) 347.
[52] M. Kotzian, N. Roesch, M.C. Zerner, Theor. Chim. Acta 81 (1992) 201.
[53] M. Kotzian, N. Roesch, M.C. Zerner, Int. J. Quant. Chem. (1991) 545.
[54] J.A. Pople, D. Beveridge, P.A. Dobash, Chem. Phys. 47 (1967) 2026.
[55] T.H. Huang, K.E. Reickhoff, E.M. Voigt, J. Chem. Phys. 77 (1982) 3424.
[56] T.H. Huang, K.E. Reickhoff, E.M. Voigt, J. Phys. Chem. 85 (1981) 3322.
[57] J.C. Donini, B.R. Hollebone, A.B.P. Lever, Progr. Inorg. Chem. 22 (1977) 225.
[58] R.M. Hochstrasser, C. Marzzacco, J. Phys. Chem. 49 (1968) 971.
[59] D.W. Clack, J.R. Yandle, Inorg. Chem. 11 (1972) 1738.
[60] L.D. Rollman, R.T. Iwamoto, J. Am. Chem. Soc. 90 (1968) 1455.
[61] W.A. Nevin, M.R. Hempstead, W. Liu, C.C. Leznoff, A.B.P. Lever, Inorg. Chem. 26 (1987) 570.
[62] W.A. Nevin, W. Liu, S. Greenberg, M.R. Hempstead, S.M. Marcuccio, M. Melnik, C.C. Leznoff, A.B.P. Lever, Inorg. Chem. 26 (1987) 891.
[63] A. Louati, M. El Meray, J.J. Andre, J. Simon, K.M. Kadish, M. Gross, A. Giraudeau, Inorg. Chem. 24 (1985) 1175.
[64] A. Giraudeau, A. Louati, M. Gross, J.J. Andre, J. Simon, C.H. Su, K.M. Kadish, J. Am. Chem. Soc. 105 (1983) 1175.
[65] N.M. Golovin, P. Seymour, K. Jayaraj, Y. Fu, A.B.P. Lever, Inorg. Chem. 29 (1990) 1719.
[66] A.B.P. Lever, J.P. Wilshire, Inorg. Chem. 17 (1978) 1145.
[67] R.E. Linder, N.S. Rowland, N.S. Hush, Molec. Phys. 21 (1971) 417.
[68] C.M. Guzy, J.B. Raynor, L.P. Stodulski, M.C.R. Symons, J. Chem. Soc. A 10 (1969) 997.

[69] D.W. Clack, N.S. Hush, I.S. Woolsey, Inorg. Chim. Acta 19 (1976) 129.
[70] A.B.P. Lever, S. Licoccia, P.C. Minor, B.S. Ramaswamy, S.R. Pickens, J. Am. Chem. Soc. 103 (1981) 6800.
[71] T. Nyokong, Z. Gasyna, M.J. Stillman, Inorg. Chim. Acta 112 (1986) 11.
[72] E.A. Ough, M.J. Stillman, J. Porphyrins Phthalocyanines (2001) submitted.
[73] J. Mack, M.J. Stillman, J. Porphyrins Phthalocyanines 5 (2001) 67.